Journal of Glaciology

Article

Cite this article: Scarchilli C et al. (2020). Characterization of snowfall estimated by in situ and ground-based remote-sensing observations at Terra Nova Bay, Victoria Land, Antarctica. *Journal of Glaciology* **66**(260), 1006–1023. https://doi.org/10.1017/jog.2020.70

Received: 27 March 2020
Revised: 28 July 2020
Accepted: 28 July 2020
First published online: 1 October 2020

Key words:
Accumulation; ice in the atmosphere; remote sensing; surface mass budget; wind-blown snow

Author for correspondence:
Claudio Scarchilli,
E-mail: claudio.scarchilli@enea.it

cambridge.org/jog

Characterization of snowfall estimated by in situ and ground-based remote-sensing observations at Terra Nova Bay, Victoria Land, Antarctica

Claudio Scarchilli[1], Virginia Ciardini[1], Paolo Grigioni[1], Antonio Iaccarino[1], Lorenzo De Silvestri[1], Marco Proposito[1], Stefano Dolci[2], Giuseppe Camporeale[3], Riccardo Schioppo[4], Adriano Antonelli[5,6], Luca Baldini[7], Nicoletta Roberto[7], Stefania Argentini[7], Alessandro Bracci[7,8] and Massimo Frezzotti[9]

[1]Laboratory for Observations and Measurements of the Environmental and Climate (SSPT-PROTER-OEM), ENEA, Rome, Italy; [2]Antarctic Technical Unit – Logistics Service (UTA-LOG), ENEA, Rome, Italy; [3]Institute for Electromagnetic Sensing of the Enviroment (IREA), CNR, Naples, Italy; [4]Laboratory of Manufacturing Technologies of photovoltaic cells (DTE-FSD-TEF), ENEA, Rome, Italy; [5]European Commission DG Joint Research Centre Directorate for Energy, Transport and Climate Energy Storage Unit, Petten, The Netherlands; [6]Laboratory of Smart Cities and Communities (DTE-SEN-SCC), ENEA, Ispra, Italy; [7]Institute of Atmospheric Science and Climate (ISAC), CNR, Rome, Italy; [8]Department of Physics and Astronomy, University of Bologna, Bologna, Italy and [9]Department of Science, University of 'Roma Tre', Rome, Italy

Abstract

Knowledge of the precipitation contribution to the Antarctic surface mass balance is essential for defining the ice-sheet contribution to sea-level rise. Observations of precipitation are sparse over Antarctica, due to harsh environmental conditions. Precipitation during the summer months (November–December–January) on four expeditions, 2015–16, 2016–17, 2017–18 and 2018–19, in the Terra Nova Bay area, were monitored using a vertically pointing radar, disdrometer, snow gauge, radiosounding and an automatic weather station installed at the Italian Mario Zucchelli Station. The relationship between radar reflectivity and precipitation rate at the site can be estimated using these instruments jointly. The error in calculated precipitation is up to 40%, mostly dependent on reflectivity variability and disdrometer inability to define the real particle fall velocity. Mean derived summer precipitation is ~55 mm water equivalent but with a large variability. During collocated measurements in 2018–19, corrected snow gauge amounts agree with those derived from the relationship, within the estimated errors. European Centre for the Medium-Range Weather Forecasts (ECMWF) and the Antarctic Mesoscale Prediction System (AMPS) analysis and operational outputs are able to forecast the precipitation timing but do not adequately reproduce quantities during the most intense events, with overestimation for ECMWF and underestimation for AMPS.

1. Introduction

Snowfall (SF) plays a key role in the hydrological cycle of the Antarctic Ice sheet. Understanding its variability is one of the challenges of polar research necessary for determining the contribution of the ice sheet to sea-level rise (IPCC, 2013). The mass balance of the ice sheet is defined as the net balance between the mass of accumulated snow at the surface and mass lost through ice discharge at ice-sheet boundaries and basal melting. The accumulated snow, or the surface mass balance (SMB), represents the net budget between the SF and the mass lost through the effect of post depositional processes, mainly driven by winds (Scarchilli and others, 2010; Frezzotti and others, 2013; Palm and others, 2017). SF represents the main positive component of SMB and drives its variability at continental/regional scales (Monaghan and others, 2006). Climate models predict an SF increase in a warmer atmosphere, principally over the coastal areas of the ice sheet (Palerme and others, 2017); however, it is still debated whether this modeled SF enhancement really occurred during the most recent decades preceding the present time and how it may have counteracted sea level rise during that time period (Monaghan and others, 2006; Frezzotti and others, 2013; Thomas and others, 2017; Lenaerts and others, 2018; Medley and Thomas, 2019).

SF ranges between 20 and 1000 mm water equivalent (w.e.) a^{-1} (Palerme and others, 2014), varying strongly between Antarctic regions, and markedly decreasing from coasts toward the high plateau. Few direct SF measurements have been collected in Antarctica due to the very harsh conditions (Souverijns and others, 2018). Evaluation of solid precipitation estimates has been historically obtained from model outputs (van Wessem and others, 2018; Agosta and others, 2019), and from indirect methods based on the evaluation of the other SMB components (Frezzotti and others, 2013; Favier and others, 2017). More recently, data products from CLOUDSAT satellite are also being used to improve SF estimation (Palerme and others, 2014; Milani and others, 2018). However, both retrieval from satellite data (Palerme and

others, 2014; Souverijns and others, 2018; Lemonnier and others, 2019) and model outputs are affected by large uncertainties due to the lack of experimental data, which are essential to validate and improve the precipitation parameterizations and estimates from models or minimizing the impact of intrinsic limitations of the measurements techniques (e.g. CloudSat ground clutter; Maahn and others, 2014).

Ground-based remote-sensing instrumentation based on radar technology can be a valuable tool for obtaining estimates of SF at a site (Gorodetskaya and others, 2015). However, to define a robust relationship between radar estimates and true precipitated quantities, a variety of information on falling particles should be known or assumed. Only a few research efforts have been carried out in Antarctica using radar due to the high logistic and instrumental costs. Konishi and others (1992) obtained a relation between SF quantity and vertical radar reflectivity profiles for three SF events at Syowa station (SW, Fig. 1), comparing the atmospheric profiles sampled by a vertically pointing radar with semi-automatic measurements of snowflake characteristics at the surface. During the last decade, the development of new low budget radar profilers and the rising importance of algorithms for estimation of SF amounts revived the interest in solid precipitation assessment using radar techniques (Maahn and Kollias, 2012), corroborated also by the promising results obtained in sites characterized by harsh conditions. Gorodetskaya and others (2015) showed (at Princess Elisabeth station, PE, Fig. 1) the potential of the synergetic use, of ground-based remote-sensing (at microwave and visible frequencies) and surface measurements, for qualitatively distinguishing cloud characteristics (ice, liquid-phase) and precipitation quantities. Souverijns and others (2017) revisited this research using the same vertical pointing radar and a disdrometer (Newman and others, 2009) placed at the PE station. They obtained a relation between radar reflectivity and SF rate ($Ze–SF_{RATE}$) and proposed a detailed analysis of explicit and implicit errors laying on its usage. At the same time, Grazioli and others (2017a) published an estimation of SF quantities and a characterization of falling particles for Dumont d'Urville station (DDU, Fig. 1) using an in situ vertically pointing radar in conjunction with a weighing snow gauge.

At the present time, there are only a few sites in Antarctica that are equipped with radar and other up-to-date facilities which are crucial to the proper characterization of precipitation events. New sampling sites are needed in order to give robustness to SF estimates and to better understand interactions between the atmosphere and the cryosphere (Souverijns and others, 2018). In particular, it is desirable to better constrain the real impact of precipitation on the SMB, especially over the coastal areas where wind-driven processes during and after the deposition can remove more than 80% of the precipitated snow (Frezzotti and others, 2007; Scarchilli and others, 2010; Grazioli and others, 2017b).

The Polar Prediction Project (PPP) is a 10-year (2013–2022) program of the World Meteorological Organization (WMO) with the aim of promoting cooperative international research for improving weather and environmental prediction services for the polar regions, on different time scales. The Year of Polar Prediction (YOPP) is one of the key elements of PPP. Its principal goal is to improve the prediction capabilities for the polar regions, by coordinating special observing periods with enhanced observing modeling and verification activities. The 2018–2019 summer Antarctic campaign was the special observing period of the YOPP program for the Southern Hemisphere with an enriched observational and modeling campaign over the whole Antarctic continent.

The Italian polar research community has made a great effort to develop products useful for achieving the YOPP main targets. In this framework, the present paper is focused on the quantification of the total precipitated mass, the characterization of the local flow and its interaction with precipitation at the Italian Mario Zucchelli Station (MZS) placed in a steep coastal area of the Victoria Land facing the Ross Sea (Fig. 1). Moreover, the study addresses the evaluation of various reanalysis product and model forecasts, in order to correctly model precipitated quantities during events that occurred during the 2018–2019 YOPP intensive campaign and the three previous austral summer campaigns (2015–16, 2016–17, 2017–18). Measurements were obtained with a vertical pointing radar, an optical disdrometer, a weighing pluviometer, radiosounding profiles and an automatic weather station (AWS). Part of this instrumentation was expressly improved for the YOPP Southern Hemisphere Special Observing Period. The present paper is structured as follows: in the first section, a description of the site and the instrumentation used is reported. In the second, the methodology applied is detailed. In the third and fourth sections, the results are presented, discussed and compared with model outputs, in order to highlight peculiar characteristics of precipitation events in the area and to assess the ability of models to reproduce the estimated quantities.

2. Site and dataset

Terra Nova Bay area (TNB) is located along the coast of Northern Victoria Land on the western Ross Sea between Cape Washington and the Drygalski Ice Tongue and comprising the Nansen Ice Sheet (Fig. 1). The Italian summer Station Mario Zucchelli (74° 41′S, 164°07′E, 15 m a.s.l) is located downwind of the Northern Foothills along the coast above a mostly de-glaciered area.

SMB over the TNB area, obtained from ice core data at several sites, is about 150–270 kg m^{-2} a^{-1} (Stenni and others, 2000). The core sites are not significantly influenced by katabatic wind scouring. Direct measurements of SF are not yet available. Despite the plateau escarpment above the TNB area is windy, and characterized by massive and recognizable events of blowing snow driven by the wind, the MZS site is less affected by blowing snow during katabatic events because the ice particles lifted up by the wind over the plateau are completely sublimated before reaching the coast (Scarchilli and others, 2010).

2.1. Instrumentation available

A large set of instruments has been installed in the area of TNB and at MZS during the various Italian expeditions in Antarctica. The Italian Antarctic Meteo-Climatological Observatory (IAMCO, http:\\www.climantartide.it) provides standard meteorological measurements collected in the area by different AWS operating year round, since 1987, radio-sounding profiles and additional laser-optical instruments (e.g. ceilometer and visibilimeter) installed seasonally at MZS. Meteorological data used in the analysis were obtained from two AWSs, named 'Eneide' and 'Lucia', and radiosounding. Eneide is placed at 82 m a.s.l., 300 m from MZS with wind speed/direction sensors at 10 m above ground, whereas Lucia, a mast 3 m in height, is placed on the Larsen Glacier, 80 km from MZS at 74°57′S, 161°46′E, ~1250 m a.s.l. at the edge of the plateau escarpment and within the katabatic flow channel that drains air from the plateau toward the coast (Fig. 1). The radiosounding launches are deployed at MZS from middle October to the first days of February twice per day (at hours 00.00 and 12.00 UTC) a few meters from the Eneide AWS (Fig. 1), using a Digicora Vaisala system, with RS91 Vaisala sounds. Each radiosounding profile was vertically averaged every 50 m in order to obtain profiles comparable with each other at the same altitude.

A Thies CLIMA laser disdrometer, managed by IAMCO, hereafter LPM_{OASI}, has been operational since December 2014 on the

https://doi.org/10.1017/jog.2020.70 Published online by Cambridge University Press

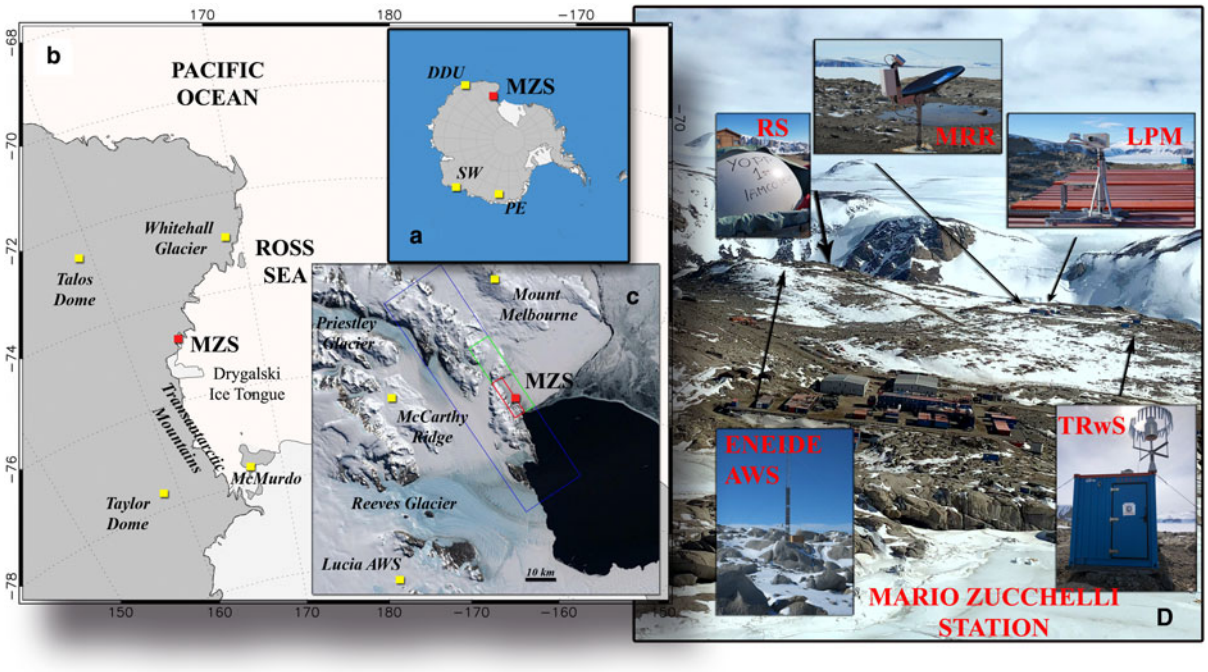

Fig. 1. Map of the studied area. (a) Map of Antarctica with the position of Mario Zucchelli (MZS), Princess Elisabeth (PE), Dumont d'Urville (DDU) and Syowa (SW) stations. (b) Location and coastal profile of the area of Victoria Land (Antarctica). (c) A clear sky Aqua MODIS image (250 m resolution) of the Terra Nova Bay (TNB) area in Victoria Land. Red and yellow points indicate the positions of Mario Zucchelli Station (MZS), automatic weather station (AWS) Lucia (Larsen Glacier), McCarthy Ridge ice core site and Mount Melbourne, respectively. Colored rectangles show model nearest mesh of ECMWF ERA Interim, ERA5 and Operational products (green, blue and red, respectively) including MZS (red square). (d) Photo of MZS with positions and images of the instruments (AWS Eneide, MRR Metek radar, LPM_{OASI} Thies Clima optical disdrometer and TRwS MPS weighing snow gauge, and radiosounding launcher) used for this study.

roof of a building placed in the outskirts of MZS (Fig. 1) at ~10 m above the ground. The disdrometer can simultaneously count and measure the size and fall velocity of hydrometeors (Frasson and others, 2011). The optical sensor generates a parallel horizontal light beam, and when a particle falls through it, the receiving signal is reduced and the amplitude and the duration of the reduction are related to the particle size and the fall speed, respectively. The instrument produces a data matrix containing the number of particles counted over 1 min intervals in relation to their size and fall velocity. Due to the limited datalogger space storage, during the former two campaigns, only one LPM_{OASI} data matrix (with 1 min integration period) was stored every 5 min, whereas since November 2017, when a new datalogger has been added to the system, it has been possible to acquire both the full (every minute) and the lower (one sample every 5 min) resolution data.

A Micro Rain Radar 2 (MRR) was installed in MZS at the end of November 2015 on the same roof but a few meters away from the LPM_{OASI} (Fig. 1). The MRR is an easily deployable and inexpensive, vertically pointing radar, manufactured by Meteorologische Messtechnik GmbH (Metek). MRR is extremely suitable for measurements in harsh and unmanned environments (Gorodetskaya and others, 2015) and it records Doppler velocity spectra every 10 s at 32 range gates, whose spacing can be set by the user. At MZS, such gate spacing was set to 100 m allowing the profiler to sound heights ranging from 100 to 3100 m above the surface. Data from the first two gates were disregarded from the analysis due to near-field effects. The raw K-band power spectra, collected by the MRR, were processed applying the method proposed by Maahn and Kollias (2012) to correct for noise and aliasing effects, making them suitable for snow observation.

A Total Rain weighing Sensor (TRwS) manufactured by MPS system was installed during the 2018–2019 campaign within the YOPP observing period, a few tens of meters from the MRR and LPM_{OASI} (Fig. 1). The TRwS is a total rain/SF weighing gauge with an orifice area of 400 cm^2, a depth accuracy of 0.01 mm of w.e. and a 1 min sampling time resolution (Savina and others, 2012). The TRwS was protected by an alter shield in order to minimize wind effect over the accumulation inside the instrumentation. The system continuously sampled precipitation quantities at the site from 1 December 2018 to 30 January 2019.

Finally, visual observations of meteorological conditions (VO) at MZS were routinely carried out all day long during the expeditions by two Italian Air Force weather forecasters in the role of observers. The VOs include SYNOP messages, recorded at 00.00, 06.00, 12.00 and 18.00 h UTC, OBSERVATIONS and METAR messages sampled on an hourly basis. SYNOP were fully recorded, whereas, some discontinuities are present for the other messages, especially during local night-time hours (06.00–18.00 UTC).

In the presented analysis, 1 min MRR, AWS and TRwS measurements were averaged over 5 min while the LPM_{OASI} data acquired every 5 min is not averaged. Time average and std dev. of variables spanning various orders of magnitude such as radar reflectivity are computed as an arithmetic average, following Fabry (2015, 241). Radar, disdrometer and snow gauge data at 5 min, sampled at MZS in four expeditions, 2015–16, 2016–17, 2017–18 and 2018–19 during the summer months (November–December–January) are available at https://doi.org/10.1594/PANGAEA.921490 and at 'www.climantartide.it'.

2.2. Data from atmospheric reanalysis and Operational Forecasts

Many global and regional models but also atmospheric reanalysis have been used to characterize Antarctic SF climatology and its main features (Lenaerts and others, 2016; Palerme and others, 2017a; van Wessem and others, 2018; Agosta and others, 2019). In the present paper, we compare accumulated SF and total precipitation (TP) from ERA Interim (ERAin), ERA5 and

https://doi.org/10.1017/jog.2020.70 Published online by Cambridge University Press

Operational Forecast (OP) datasets, provided by the European Centre for Medium-Range Weather Forecasts (ECMWF) and the precipitation fields produced by the Antarctic Mesoscale Prediction System (AMPS), with the SF quantities obtained from field measurements. The choice of different reanalysis products and model forecasts is related to the increased knowledge that is necessary for both improving forecast ability of operational models inside the YOPP main target and testing model reference in the area of climate research. In this framework, the OP and AMPS represent the references for operative decisions, weather forecasting and air flight schedules over most of the Antarctic area, especially for the Ross Sea area. Moreover, the ERAin reanalysis (Dee and others, 2011) was considered the most reliable product over the Antarctic area (Bromwich and others, 2011; Palerme and others, 2017a) whereas the ERA5, the newest reanalysis dataset of the ECMWF (Hersbach and Dee, 2016), is the upgraded version of the ERAin, and it was scheduled to completely replace the ERAin at the end of 2019.

The ERAin is a reanalysis archive of the global atmosphere covering the period from 1979 to present; it is based on the cycle 31r2 of the IFS model and it is characterized by a spatial resolution of data of ~80 km (T255 spectral). The ERAin dataset, considered for the comparison, is the 3-hourly forecast initialized from analyses at 00.00 h UTC. The ERA5 is a reanalysis based on the IFS model cycle 41r2. It covers the period from 1979 to present and is characterized by a higher spatial and temporal resolution (31 km globally) and a newer cloud scheme (Forbes and others, 2011, 2014) with respect to ERAin. The ERA5 data used consist of hourly forecasts, 12 h long and initialized twice daily from analyses at 06.00 and 18.00 h UTC. Lastly, the Operational archive is characterized by the narrower grid (T1279 spectral, ~10 km). Fields used are 24 h forecasts with 1 h time steps from the 00.00 h UTC analysis. The OP runs with the up-to-date IFS model; then the output fields are based on the latest version of microphysics parameterization. However, those could not be consistent with each other due to the continuing evolution of the model.

AMPS dataset is made using the Weather Research and Forecasting model (WRF) modified for use in the Polar Regions (Bromwich and others, 2013). The analyzed data are the +24 h forecast of TP from 00.00 h UTC. The model was applied to the so-called 'Domain 5', encompassing the area between McMurdo Sound and TNB and part of the Ross Ice Shelf, with a horizontal resolution of 1 × 1 km (http://polarmet.osu.edu/AMPS/).

For each precipitation dataset from model forecasts and reanalysis, the four nearest grid points at the MZS position time series were extracted and the average and the std dev. were calculated in order to define the mean precipitation quantities and their variability over the smallest model mesh grid encompassing the MZS site.

2.3. Back-trajectories

The Hybrid Single-Particle Lagrangian Integrated Trajectory (HYSPLIT) model, developed by NOAA and Australia's Bureau of Meteorology (Stein and others, 2015), was used to identify the provenance of the air masses ending in MZS. Five-day back-trajectories were computed hourly from 6 November to 31 January, covering completely the four-campaign time range and arriving at six different altitudes (500, 1000, 1500, 2000, 3000 and 4000 m) over the site. The model was initialized with the meteorological data fields provided by the ECMWF Operational analysis archive with a regular grid of 0.125° × 0.125°. Errors in the trajectory calculations after 3 d are estimated in the range 10–30% of the travel distance (Scarchilli and others, 2011). A K-cluster mean method (Scarchilli and others, 2011) based on air parcel longitude, latitude, height over the terrain and thermodynamics conditions along the path was applied in order to sort back-trajectory ensemble in five clusters and highlight the different patterns of transport toward the site. The choice of cluster number was almost subjective, but tests with different cluster numbers did not reveal different atmospheric pathways.

3. Methods

3.1. Ze–SF_{RATE} relationship calculation

In this paper, an equivalent Reflectivity (Ze)–precipitation rate (SF_{RATE}) relationship optimized for the MZS site is developed, using a combination of radar and disdrometer products, in order to estimate the quantities of precipitation. Various authors have confirmed the validity of this approach for SF estimation (Huang and others, 2010; Souverijns and others, 2017). The relationship is reliable in almost all meteorological conditions when other instrumentation deployed to precipitation measurement can fail (e.g. snow gauge and/or disdrometer). Moreover, it is intrinsically linked to the mean atmospheric characteristics during precipitation events and comparison between the relationship calculated for different sites can give information on similarities or differences between atmospheric conditions above the studied areas. The Ze–SF_{RATE} relationship has the classical power law form

$$SF_{RATE} = A\ Ze^{B}, \tag{1}$$

where the parameters A and B are evaluated by means of fitting the Ze and SF_{RATE} calculated from disdrometer measurements in the following way:

$$Ze = 10^{18}\frac{\lambda^4}{\pi^5|K|^2}\int_{D_{min}}^{D_{max}}\sigma_b(D)N(D)dD \quad [mm^6\ m^{-3}], \tag{2}$$

$$SF_{RATE} = \frac{3600}{\rho_w}\int_{D_{min}}^{D_{max}} m(D)v(D)N(D)dD \quad [mm\ h^{-1}], \tag{3}$$

where λ is the MRR wavelength in m, $|K|^2$ is related to the dielectric constant of liquid water (the value conventionally used is 0.92, Atlas and others, 1973), σ_b is the backscatter cross-section[m^2] at 24 GHz, $N(D)$ is the particle size distribution [m^{-4}], ρ_w is the density of liquid water [g cm^{-3}], $m(D)$ is the mass (g), and $v(D)$ the terminal fall velocity [m s^{-1}], all functions of the maximum particle dimension. The particle size distribution $N(D_i)$ in size class i is calculated from raw particle numbers measured by the optical disdrometers as

$$N(D_i) = \sum_{j=1}^{Nv}\frac{n_{ij}}{A_s\Delta t v_j \Delta D_i} \quad [m^{-3}mm^{-1}] \tag{4}$$

(Chen and others, 2016) where N_v is the number of disdrometer velocity class intervals, n_{ij} is the number of particles sampled in each size (i) and velocity (j) class interval, A_s and ΔD_i are the disdrometer measuring area [m^2] and the width of each diameter bin [mm], respectively. Δt is the time interval [s] and vj is the fall velocity of each velocity class [m s^{-1}].

The measurement accuracy of optical-disdrometers may be affected by instrumental and external issues, or a mixture of these, such as spatial variability of laser beam intensity (Frasson

https://doi.org/10.1017/jog.2020.70 Published online by Cambridge University Press

and others, 2011), strong winds (Friedrich and others, 2013) and 'margin faller' particles (Yuter and others, 2006). In order to minimize these problems, particles with fall velocity greater than a threshold value are removed. The speed limit for each D_i was set equal to the rain terminal velocity, calculated from the velocity–diameter relationship $V_i = 9.65 - 10.3\ e^{(-0.6\ D_i)}$ (Atlas and others, 1973), increased by +50% (Chen and others, 2016). The threshold cuts ~80% of the total detected particles that mostly fall within the first three diameter bins because of anomalous fall velocities, the 95% of the total volume sampled is conserved.

The backscatter cross-section, representing particle scattering properties, is evaluated using the self-similar Rayleigh-Gans approximation theory (SSRGA). This is a fairly simple method based on the 1-D description of the structure of a snow particle (Hogan and Westbrook, 2014; Hogan and others, 2017). The SSRGA derives the scattering properties for an ensemble of particles, a description that is much closer to real radar sampling volumes than it is to a description based on single-particle scattering. Moreover, it is considered more accurate than the soft spheroid approximation obtained with T-Matrix (Mishchenko and others, 1996) and is less computationally expensive than more complex single scattering methods such as discrete dipole approximation (Draine and Flatau, 1994).

Both SF_{RATE} and Ze depend on $m(D)$, explicitly the former, implicitly the latter, through the backscatter coefficient (Hogan and Westbrook, 2014). The characterization of snowflake mass is one of the most difficult tasks in quantitative estimation because it depends on the evolution of the precipitation system and its unique thermodynamic characteristics. Various authors presented different relationships relating mass and particle diameter in the form $m = \alpha\ D^{\beta}$ (Locatelli and Hobbs, 1974). No information is still available at the MZS site on precipitated particle mass and, consequently, up to the present time mass is estimated with a parameterization-based approach (Fontaine and others, 2014).

Firstly, the model reflectivity (hereafter Ze_app) is calculated via Eqn (2) where the backscatter coefficient dependence on mass is expressed as in Eqn (12) from Hogan and Westbrook (2014), where the ice volume V in the particles is parametrized as $V = \frac{m}{\rho_{ice}} = \frac{\alpha\ D^{\beta}}{\rho_{ice}}$ with ρ_{ice} the ice density (0.917 [g cm^{-3}]). The particle distribution is the one measured by the disdrometer. Ranging β systematically over 201 values between 1 and 3 (Fontaine and others, 2014) with a step size of 0.01, a set of Ze_app values is obtained for each time step. Then α is subsequently evaluated as the one that minimizes the difference, in a least-squares sense, between the Ze measured by MRR at 300 m (Z_{MRR}) above the ground and the Ze_app, over a 15 min time window (three points). The choice to vary β and set α is due to the constrained range of values of the former whereas the latter shows values spanning various orders of magnitude (Fontaine and others, 2014). The procedure generates the matrix $m(D, t, \beta)$, $Ze(t, \beta)$ as a function of time (t), the 201 value of β and the diameter (D). Using Eqn (3) with $m(D, t, \beta)$ it is possible to calculate $SF_{RATE}(t, \beta)$. In order to exclude physically impossible solutions, those for $m(D0)$, being $D0$ the median diameter of particles, correlated to a bulk particle density greater than ice density are discharged for each time interval. The bulk particle density is qualitatively evaluated as $\rho = \frac{m(D0)}{V}$ (Brandes and others, 2007) where V is the volume of a particle approximated as a spheroid with major axis equal to $D0$ and aspect ratio equal to 0.6 (Hogan and Westbrook, 2014).

For each time step, mean values of $Ze(t, \beta)$, $SF_{RATE}(t, \beta)$ and $m(D, t, \beta)$ are calculated by means of averaging with respect to β (hereafter $Ze^{m}(t)$, $SF^{m}_{RATE}(t)$ and $m^{m}(t)$, respectively). Uncertainties of SF^{m}_{RATE} and Ze^{m} are assumed to be the std dev. Comparison between Ze^{m} and Z_{MRR} shows a linear relation, with slope and intercept equal to 0.94 and −0.5 dBz, respectively, and a reasonable correlation (R^2~0.7) (not shown).

Parameters A and B of the Ze–SF_{RATE} relationship (1) are obtained through a linear regression analysis between SF^{m}_{RATE} and Ze^{m} values using a non-linear least-square fitting routine (Markwardt, 2009). The main regression analysis is based on the SF^{m}_{RATE} and Ze^{m} calculated with all the disdrometric data with one sample every 5 min and a Z_{MRR} 5 min average, collected during the four campaigns (each from November to January). However, we exclude time steps where any of the following conditions apply:

- disdrometer or MRR data missing
- wind speed at 10 m >7 m s^{-1}
- Z_{MRR}, and calculated Ze^{m} lower than −5 dBz
- calculated SF^{m}_{RATE} lower than 0.01 mm h^{-1}
- Z_{MRR} at 300 m >−5 decibel (dBz) but lower than −5 dBz between 400 and 1000 m

in order to exclude, from the regression, the contamination by external factors (such as snow transport) or extreme events such as strong horizontal wind, incompleteness of MRR reflectivity measurements and insufficient numbers of falling particle events (Souverijns and others, 2017). Particularly, the choices of −5 dBz and 0.01 mm h^{-1} are connected to the MRR's limited sensitivity (Maahn and Kollias, 2012), whereas the 7 m s^{-1} value is chosen following the results of Li and Pomeroy (1997) for wind-driven dry snow transport. Finally, the last condition is selected in order to completely disregard snow transported from well-developed precipitation events. The remaining dataset is hereafter reported as selected cases (Ω). Indeed, with the same exclusion conditions, the regression is applied also to the same datasets but considering only specific campaign time periods. Moreover, it is also applied to the dataset based on disdrometric measurements sampled every 1 min during the last two campaigns in order to understand whether the subsampling could bias the results.

Finally, in order to obtain SF from the measured MRR reflectivity, the Ze–SF_{RATE} formula found is inverted:

$$SF_{RATE} = \left(\frac{Ze}{A}\right)^{\frac{1}{B}} \tag{5}$$

and the result multiplied for the time window. Uncertainty in SF_{RATE} is evaluated using the error propagation theory based on the A, B and Z_{MRR} errors. The two-parameter errors are calculated from the regression analysis whereas the std dev. of Z_{MRR} over the 5 min mean is considered as the error in radar reflectivity.

3.2. Error evaluation of disdrometer measurements

Since the laser disdrometer instrument is designed to measure spherical/spheroidal liquid particles, the instrument has numerous limitations when used to perform measurements on solid precipitation. Battaglia and others (2010) detailed a number of constraints of a specific instrument of this type, the OTT Parsivel disdrometer, for detecting snow and ice particles. Mainly, the constraints are related to the assumptions used for retrieval, such as the fixed spheroidal shape of particles, the absence of horizontal transport through the laser beam, the presence of a single particle in the beam at a certain moment, or instrumental observation limitations such as particles that are only partially seen by the measurement beam. In particular, the Parsivel instrument measures an apparent particle diameter related to the maximum shadowed area of the particle as it passes

https://doi.org/10.1017/jog.2020.70 Published online by Cambridge University Press

through the laser beam. In a limited set of conditions where the snowflake is horizontally aligned, this measurement is equivalent to the widest horizontal dimension of the snow particle; otherwise, the apparent diameter measured represents an estimate of the widest horizontal diameter with an error ≤20% (Molthan and others, 2016). Moreover, the particle fall speed measured by the Parsivel instrument may not be accurate for a single snowflake particle, whereas, when averaged over a large number of snowflakes tend to be underestimated for a value up to 20%, especially for smaller particles (Battaglia and others, 2010).

There is no discussion in the literature of the capabilities of the Thies CLIMA disdrometer for the measurement of solid precipitation. Only a few articles have argued that the precipitation rate calculated internally is reliable with respect to snow gauge measurements on a daily basis (e.g. Zhang and others, 2015). However, the algorithm used by Thies CLIMA for SF calculation of density parameterization as a function of temperature, particle fall speed and diameter, has not yet been published (M. Hillebrecht, personal communication) and consequently is not available for use in research. However, the raw data matrix produced by the Thies CLIMA can be used, but it is reasonable to expect that its use may be subject to the same issues that apply to the use of the OTT Parsivel instrument, due to similar operating principles. Consequently, the variability of the quantity of precipitation connected to an increase/decrease of the reference values of particle dimension/velocity bins must be carefully evaluated.

The SF quantities are recalculated supposing that the mean values of the diameter and/or velocity vectors associated with each bin of Thies CLIMA data matrix are shifted by ±20%. The new calculations produced eight different time series of SF that consider all the possible permutations of system perturbation related to diameter–velocity vectors increase/decrease.

3.3. Snow gauge data treatment

The TRwS Raw SF time series is created from differences between successive weight measurements sampled every 1 min. In order to minimize spurious signal quantities measured by the TRwS but caused by re-suspended snow particles after precipitation, evaporation or vibration due to strong katabatic wind events, the approach described in Grazioli and others (2017a) is applied. Time steps at which no signal was recorded by the MRR at its lowest available gate (300 m) are considered precipitation free and any increase in the cumulative precipitation records of the snow gauge was considered as external contamination and then discarded. Moreover, a correction function dependent on wind speed and temperature based on Kochendorfer and others (2017) was evaluated (their eq. 4 with coefficients expressed in their Table 3 and based on both their single 'alter' stations) in order to mitigate biases connected to gauge snow under-catch problems at high wind velocity.

4. Results

4.1 Mean conditions during SF events at MZS

During the 2015–16, 2016–17, 2017–18 and 2018–19 summer campaigns, each during the November–December–January time window, the hourly visual observations at MZS were recorded for ∼67% of the time equally divided over the four campaigns. 87% of the observations report no significant event, 9% report precipitations observed over the MZS area, whereas the other ∼4% in the vicinity of the site. Over MZS, SF and snow grain-like precipitations are recorded 6 and 1.2% of the total observations, respectively (Fig. 2a); moreover, observers also noticed blowing/drifting as an additional condition during 13% of these specific conditions. Finally, drifting/blowing snow transport over MZS is reported ∼2% of the time, whereas the available residual observations are connected to a very few cases of mist. No liquid precipitation observations are reported in the studied dataset.

Total cloud cover density distribution over MZS shows two relative maxima (not shown) corresponding to completely clear sky or with few clouds (0–1 oktas, more than ∼30%) and to heavily broken or completely overcast conditions (7–8 oktas, ∼30%). No significant differences are present among the four campaigns (not shown), while heavy cloudy conditions are observed mostly in January compared to the other summer months (November–December, not shown). Cloud-type observations report altocumulus (Ac, 22%), stratus (St, 13%) and stratocumulus (Sc, 20%) at low levels above MZS, and prevalently CirroStratus (Cs) at higher levels (not shown). Clouds with significant vertical extent are less frequent than low/middle clouds over Antarctica, especially during summer (Adhikari and others, 2012), however very few cumulus (Cu) or tower cumulus (Tc) were observed during the 2015–2016 campaigns, and when seen were mostly during specific events. Clouds related to precipitation are mainly St or sometimes Cu or Sc (not shown).

In accordance with visual observations, the MRR sampled at the lowest radar gate (300 m) a Z_{MRR} greater than its sensitivity threshold, −5 dBz, ∼8% of the sampling time (Fig. 3a). MRR measurements are comprised of 252 large events of continuous precipitation (or with interruption <30 min) divided as 62, 46, 71 and 73 episodes during 2015–16, 2016–17, 2017–18 and 2018–19, respectively. The largest numbers of them occur during January and the smallest numbers are in November. On average, each event lasts ∼3 h but with a large std dev. (∼5.5 h) and some exceptional cases last continuously for more than 12 h.

MRR mean and median profiles of Ze, particle mean Doppler velocity (W) and spectral width (SpW) from the surface to the top of observable height (3000 m) are also shown in Figure 3. The mean Ze profile ranges from +10 (at the surface) to +5 dBz (at the top) with a variability (std dev.) less pronounced at 3 km (15–20 dBz) compared to the surface (∼30 dBz), with a progressive enhancement from 2 km downward (Fig. 3b). This is due to the high number of Ze profiles (∼35%) with signal starting to increase at the top of the measurement window, with values essentially ranging between −5 and 0 dBz at 3 km above the ground (Fig. 3a). Median Ze profile shows a similar pattern but lower values than the average due to the strong influence of the higher Ze values in the mean calculation (Duràn-Alarcòn and others, 2019). Mean W profile is constant at ∼1 m s^{-1} with a small variability up to 2 km (Fig. 3c). From 2 to ∼1 km, W slightly decreases (0.5–0.8 m s^{-1}), with an increase in its std dev., whereas for lower atmospheric layers, the mean value of W tends to increase, up to 1.2 m s^{-1}. The mean SpW profile increases monotonically downward from 0.2 at the top of the layer to 0.4 near the surface where 5 min mean values can reach 0.89. Instead, the SpW std dev. profile tends to increase with a spectrum broadening from ∼1 km toward the surface.

Figure 2b shows an average of temperature (T), relative humidity with respect to ice (RHi), wind speed (WS) and direction (WD), from radiosoundings when Z_{MRR} values were > −5 dBz and variable averages from Eneide AWS concomitant data at the ground. For ∼720 launches done during the four campaigns only, ∼10% ($N = 62$) of them occur with concomitant precipitation conditions. Mean annual 2 m T at MZS is −13.8 °C but the seasonal average can range from −21 °C during winter (June–July–August) and −3 °C in summer (December–January–February). During the 'warm' months, T values can oscillate between −20 and 0 °C (Grigioni and others, 2016). At the surface during summer precipitations, T shows a mean value of −3.5 °C

https://doi.org/10.1017/jog.2020.70 Published online by Cambridge University Press

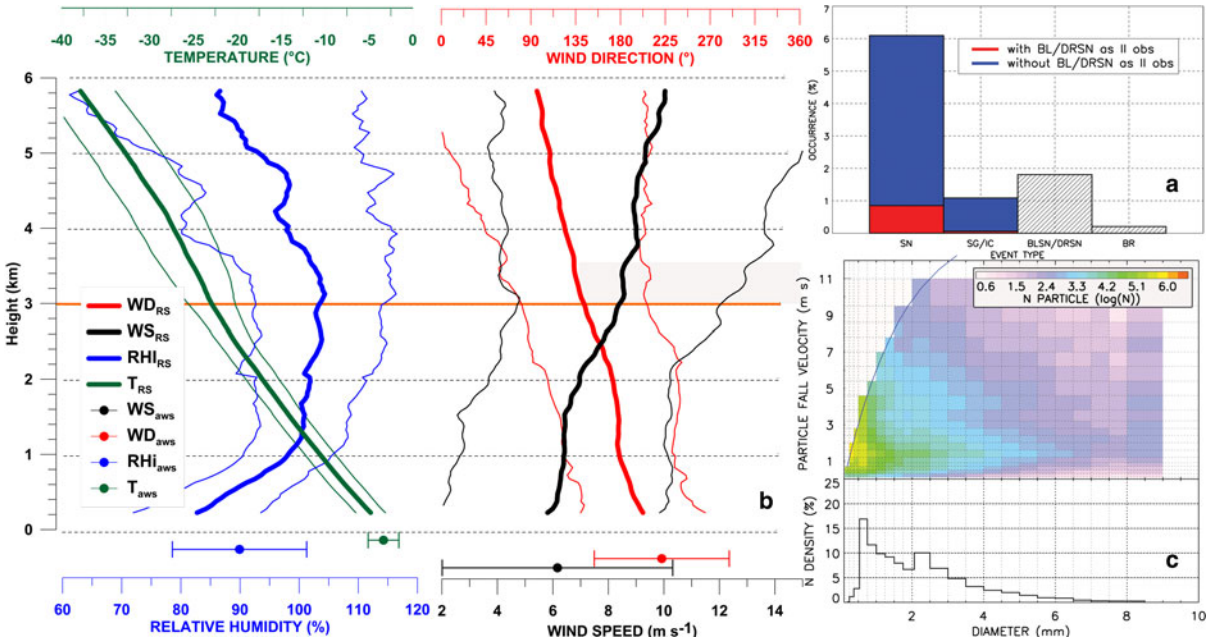

Fig. 2. (a) Mean conditions at Mario Zucchelli Station (MZS) during precipitation events. Occurrences (%) of snowfall (SN), snow or ice grain (SG/IG), blowing or drifting snow (BLSN/DRSN) and mist (BR) reported as main features by visual observation at MZS. Red and blue filled bars highlight cases with SN and SG/IG, with or without blowing snow codes as secondary features. (b) Radiosounding average profile during precipitation event (reflectivity measured by MRR at 300 m above the ground, Z_{MRR}>−5 dBz). Average temperature (*T*), relative humidity with respect to ice (RHi), wind speed (WS) and wind direction (WD), up to 6 km above the ground are highlighted in thick green, blue, black and red lines, respectively, with their related std dev. profiles (thin lines, same colors for the different parameters as for the average profiles). Concomitant *T*, RHi, WS and WD average values with their std dev., from Eneide AWS data at the surface, are represented by the colored points at height 0 (same colors for the different parameters as for the average radiosounding profiles). Orange line highlights the maximum altitude (3 km) sampled by the MRR radar. (c) Upper panel: LPM_{OASI} disdrometer data (one sample every 5 min) distribution density (colored contour) cumulative over the precipitation events (Z_{MRR}>−5 dBz) and divided for the particles fall velocity and diameter bins as defined in the original disdrometer output data matrix. Contour scale is expressed in log(*N*). Blue line highlights water droplet fall velocity +50% calculated as defined in Atlas and others (1973). Lower panel: the distribution of the median diameters (*D*0) calculated as Brandes and others (2007).

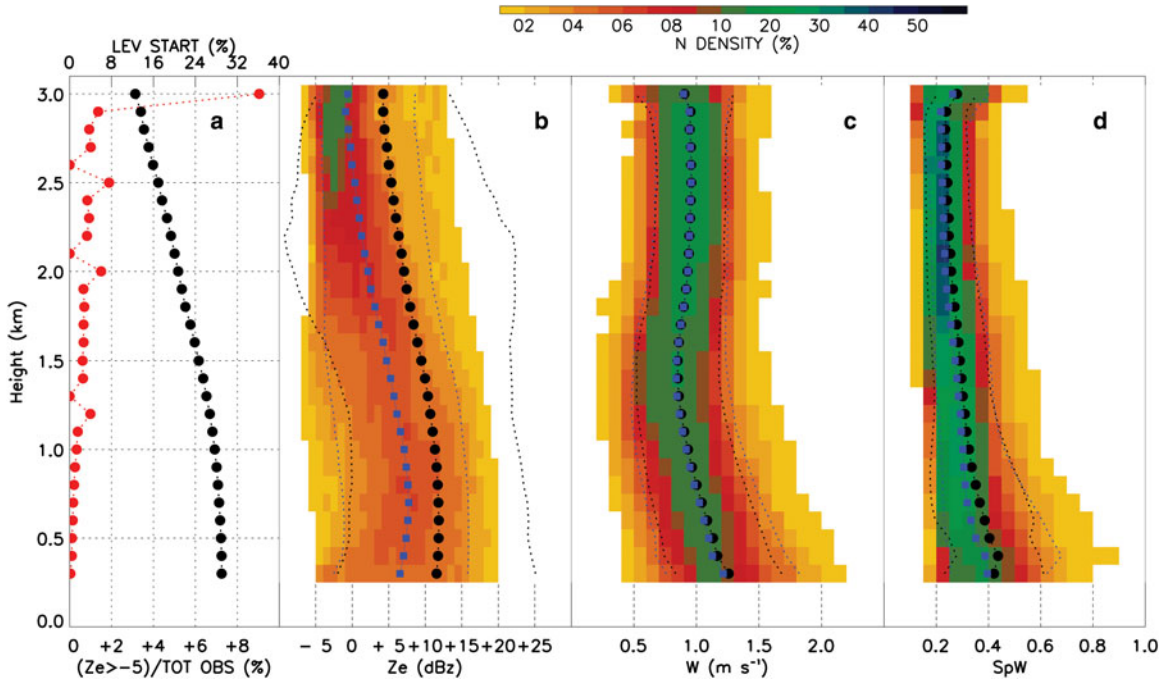

Fig. 3. Mean profiles of various MRR products. (a) Density function profiles along the height of occurrences of radar reflectivity (Ze) >−5 dBz and density function profiles of occurrence of first height where Ze is >−5 dBz is sampled (black and red lines, respectively). (b) Radar reflectivity (dBz). (c) Mean Doppler velocity (*W*, m s^{-1}). (d) Spectral width (SpW). Mean and median profiles for Ze, *W* and SpW are highlighted with filled black points and blue squares, respectively; black and blue dotted lines show the 1 std dev. of the mean profiles and 10–90 percentiles, respectively.

and on average decreases monotonically with height, up to −40 °C at ∼6 km with *T* between 0 and −10 °C in the first kilometer and between −10 and −20 mostly within the 1–3 km m a.s.l. layer. Mean RHi at the surface highlights an average value of 90% with a std dev. of 11%. Along the profile, a marked increase in RHi is apparent up to 1.5 km, above the mean value swing between saturation value (100%) up to 4.5 km and then decrease. Mean RHi maximum (∼105%) is seen over the profile between

https://doi.org/10.1017/jog.2020.70 Published online by Cambridge University Press

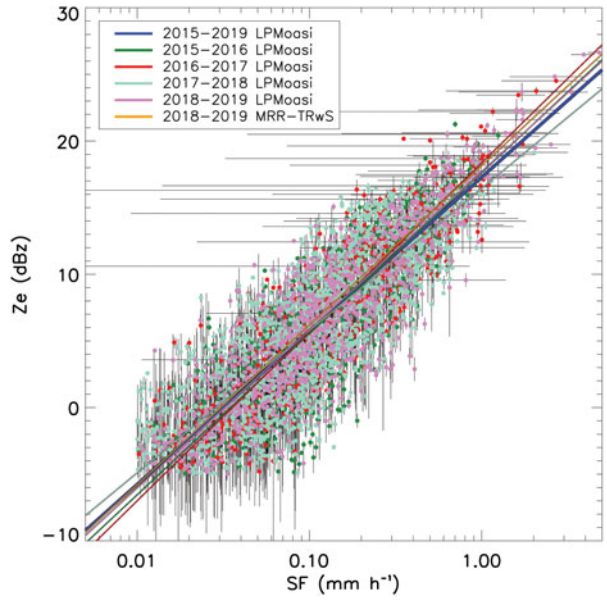

Fig. 4. Plot of precipitation rate (SF^{m}_{RATE}) and radar reflectivity (Ze^{m}) calculated from LPM_{OASI} disdrometer datasets (one sample every 5 min, see Section 3.1) for 2015–16, 2016–17, 2017–18, 2018–19 seasons (green, red, aquamarine and violet points, respectively), and their related std dev. (vertical and horizontal black lines, respectively). Black, green, red aquamarine and violet represent Ze–SF_{RATE} relationships obtained from LPM_{OASI} for all four seasons, 2015–16, 2016–17, 2017–18, 2018–19 season, respectively. Orange line highlights the Ze–SF_{RATE} calculated with the 5 min average of MRR Radar reflectivity at 300 m and TRwS snow gauge measurements.

2.5 and 3.5 km but an average condition of saturation with respect to ice is visible between 1.5 and 4 km; moreover, the RHi std dev. is large along all the profile (±15%) due to cases where a saturated condition can persist a few hundred meters above the ground. Wind conditions at MZS are principally related to air masses flowing from the plateau west of the bay, as katabatic winds, through the Reeves and/or Priestley glacier valleys into the Nansen Ice Sheet (Frezzotti, 1998). Wind speed at the surface shows an average value of 6.4 m s^{-1}, rapidly increasing until it reaches a relative maximum at ~0.4 km; then its value becomes constant up to 1.5 km where it starts to monotonically increase up to 6 km. Finally, wind direction at the surface is on average 218°, but within the first km, the wind vector turns toward 180° and then returns to a value near 200° between 1 and 1.5 km. Above, it follows a monotonic veering toward 140°, probably due to thermal wind shear.

Figure 2c also shows both (upper panel) the LPM_{OASI} raw spectra sampled during the precipitation events ($Z_{MRR} > -5$ dBz) cumulative over the particle fall velocities and diameters bins, as defined by the disdrometer original output data matrix, and (lower panel) the distribution of the median diameters ($D0$) calculated as Brandes and others (2007).

Within the errors affecting such types of optical instrumentation (see Section3.2), diameters of detected particles range from 0.16 to ~5 mm. About 90% of particles show a diameter <1 mm, with a $D0$ primary peak at 0.7 mm; but ~10% are between 1 and 3 mm, connected to the $D0$ secondary peak at 2.2 mm. Fall velocities spread between 0 and ~7 m s^{-1} but, as expected for SF precipitation, the most populated bins show a fall velocity with a marked tendency ~1–3 m s^{-1} (Locatelli and Hobbs, 1974). Moreover, particles with fall velocity between 0 and 3 m s^{-1} occur ~1 order of magnitude more often than those with fall velocity between 3 and 11 m s^{-1} (note the logarithmic scale in Fig. 2c). The disdrometer measurements can be influenced by wind speed. In total, 50–70% of the particles populating bins with fall velocities lower than 3 m s^{-1} are related to cases with WS < 7 m s^{-1}. On the other hand, most particles in bins with highest fall velocities (>3 m s^{-1}) are connected to wind speeds >7 m s^{-1} (not shown). This aspect is particularly evident for particles with small diameters which occur from 70 to 80% of the cases when WS > 11 m s^{-1} and only from 10 to 30% when WS < 7 m s^{-1} (not shown). As highlighted in Sections 3.1 and 3.2, disdrometer measurements in high wind speed regime, especially during solid precipitation events, should be considered, at least, with caution. The calculation of our Ze–SF_{RATE} relationship in the next Section is based on the selected datasets Ω calculated with a WS threshold of 7 m s^{-1} but the variability of A and B parameter is explored when the threshold in WS is relaxed.

Table 1. Values of prefactor (A) and exponent (B) of the relationship Ze–SF_{RATE} ($Ze = A \cdot SF^{B}_{RATE}$) for each dataset and period described in the text

Type	Campaign	A	B	Confidence interval 5–95% A	Confidence interval 5–95% B	N	R^2
MRR-LPM_{OASI}	2015–2019	54	1.15	51.0–56.0	1.13–1.17	3816	0.72
MRR-LPM_{OASI}	2015–2016	58.2	1.21	49.0–68.0	1.14–1.28	519	0.68
MRR-LPM_{OASI}	2016–2017	68.6	1.27	61.0–76.0	1.22–1.31	660	0.79
MRR-LPM_{OASI}	2017–2018	44.2	1.07	40.0–48.0	1.03–1.10	1658	0.64
MRR-LPM_{OASI}	2018–2019	59.0	1.19	54.0–64.0	1.15–1.22	979	0.79
MRR-LPM_{OASI} (1min data)	2017–2019	53.0	1.12	50–56	1.09–1.14	2751	0.70
MRR-LPM_{OASI} (1min data)	2017–2018	46.3	1.06	42–51	1.03–1.10	1715	0.62
MRR-LPM_{OASI} (1min data)	2018–2019	62.4	1.18	57–67	1.15–1.21	1036	0.81
MRR-TRwS	2018–2019	65.4	1.20	60–71	1.14–1.26	670	0.49

Confidence interval (5–95%) for the calculated A and B parameters, R^2 coefficient and number of measurements related to the linear regression are shown in the other columns.

4.2 Ze–SF_{RATE} relationship and related precipitated quantities

Figure 4 reports the Ze^{m} as a function of SF^{m}_{RATE} for the selected datasets Ω based on LPM_{OASI} measurements with one sample every 5 min for all of the four summer seasons we consider (see Section 3.1). The regression procedure applied to the whole Ω dataset produces the relation $Ze = 54 \cdot SF^{1.15}_{RATE}$ ($n = 3816$, $R^2 = 0.7$). The 95% confidence parameter intervals range from 51 to 56 and from 1.13 to 1.17 for A and B, respectively (Table 1). Calculated values of A based only on single-campaign subsample Ω datasets highlight large variation with respect to the value calculated with the entire datasets (+9, +27, −18 and +10% for 2015–16, 2016–17, 2017–18 and 2018–19, respectively). Conversely, the variability of B is less pronounced and has variations of +5, +10, −7 and +3% for 2015–16, 2016–17, 2017–18 and 2018–19, respectively. Standard errors in A and B are relatively small when using the whole datasets but they are more than doubled when using only single campaign datasets. Comparing the LPM_{OASI} 1 min dataset with the set with only one sample every 5 min, for the last two campaigns, do not change the results in A and B (+5% and +1%, respectively, Table 1).

In the literature, many relationships relating radar reflectivity and precipitation parameters are found but few of them are based on 24 GHz radar measurements collected during solid precipitation events and obtained specifically for Antarctic sites. Results of this study are in line with Matrosov (2007) who suggested average values of 56 and 1.2 for A and B, respectively, based on modeling using in situ data and theoretical considerations for dry SF conditions and Ka band radar frequencies. A relationship with similar prefactor ($A = 76$), comparable estimated errors, but some differences in exponent parameter ($B = 0.91$) has been found for the DDU Antarctic site (Grazioli

https://doi.org/10.1017/jog.2020.70 Published online by Cambridge University Press

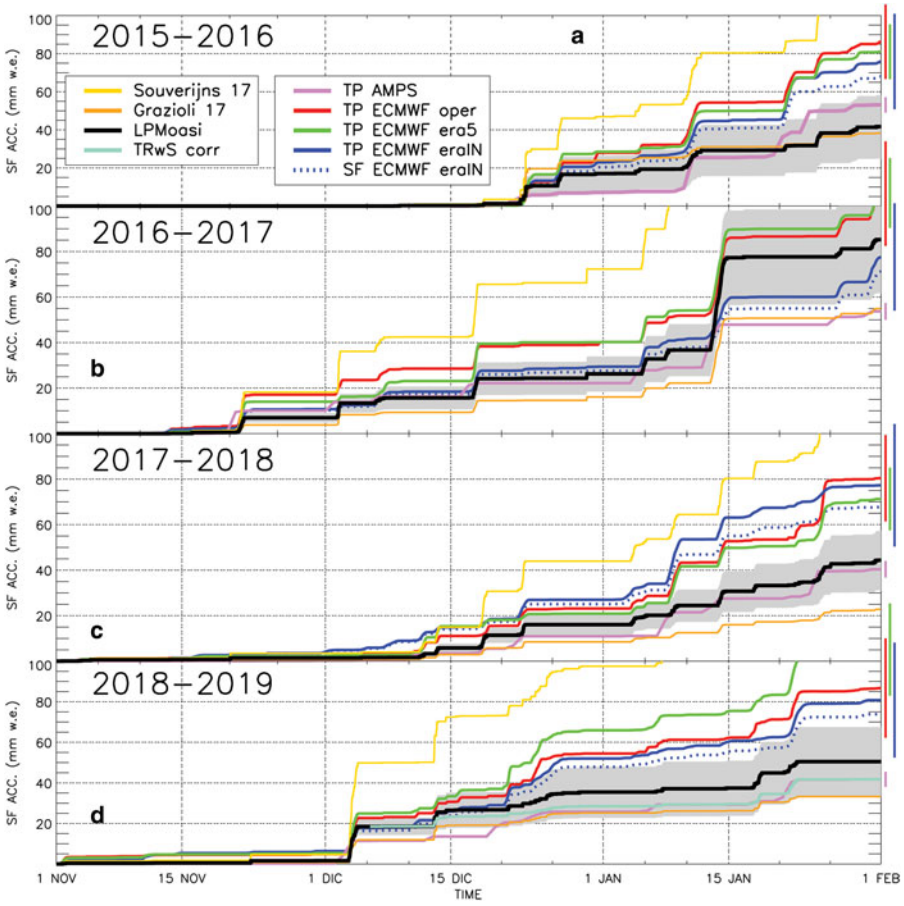

Fig. 5. Time series of accumulated precipitation quantities for the summer campaigns 2015–16, 2016–17, 2017–18 and 2018–19 (a–d, respectively). SF from the MRR reflectivity calculated with Ze–SF_{RATE} relationship obtained in this paper (see Section 4), highlighted in black line with light gray filled contour representing the associated error. Uncertainties in accumulated values are calculated by adding error propagation in Eqn (5) and variability obtained from the sensitivity analysis, based on the increase/decrease by 20% of velocity/diameter disdrometer data matrix reference bin values. SF from the MRR reflectivity calculated with Ze–SF_{RATE} relationships defined in Souverijns and others (2017) and Grazioli and others (2017a) are shown in yellow and orange, respectively; whereas the SF calculated from the TRwS snow gauge corrected for false positive, without the 3–5 December 2018 event (see Section 5), is in light blue. Accumulated total precipitation (TP) from ECMWF Operational (OP), ERA5, ERA Interim (ERAin) and AMPS are shown in red, green blue and violet solid lines, respectively. Vertical bars at the right side and in the same colors represent their associated errors at the last point. Blue dotted line is the ERAin accumulated value only for the snowfall field.

and others, 2017a). On the other hand, Souverijns and others (2017) proposed a relationship for the Antarctic PE site, based on a complex bootstrap method, with A equal to 18, ranging from 11 to 43, and B equal to 1.10 ranging from 0.97 to 1.17.

Figure 5 shows the accumulated precipitation during each summer campaign calculated with Eqn (5) applied to Z_{MRR} (SF_{MRR}). The datasets suggest a mean summer accumulated precipitation of 55.3 mm w.e. During 2018–19, 2015–16 and 2017–18, SF reached ∼45 mm w.e. (44, 46 and 53 mm w.e., respectively), whereas, during 2016–2017, the cumulative SF_{MRR} is 85 mm w.e., but a single very large, unmatched event lasting for 3 d in January alone contributed ∼40 mm w.e. Cumulative SF_{MRR} calculated with the Ze–SF_{RATE} relationship from each campaign dataset shows a variability of ∼10% with respect to the one calculated with the entire datasets (not shown). No large differences are observed between cumulative values obtained with Ze–SF_{RATE} relationship based on 1 min and 5 min sampling frequency LPM_{OASI} datasets during the 2017–18 and 2018–19 campaigns (Table 2).

Uncertainties in accumulated values are calculated by adding error connected to terms in Eqn (5) and variability obtained from the sensitivity analysis, based on a 20% increase/decrease in velocity/diameter of the disdrometer data matrix reference bin values. Values vary from ∼±28–29% (2016–17, 2017–18) to ±35–40% (2018–19, 2015–16) and are principally related to the variability of Ze measured by MRR, more than to other uncertainties. In particular, the sensitivity analysis shows that the calculated SF_{MRR} seems much more sensitive to particle fall velocity than to diameter variability. A slight difference of ±1% in SF_{MRR} values is associated with diameter bin value variation (not shown). On the other hand, varying particle fall speed brings ∼±8 to ±12% variation in SF_{MRR} values, depending on the campaigns.

Table 2. Total precipitation (mm w.e.) accumulated in each campaign calculated with different Ze–SF_{RATE} relationships or obtained by reanalysis and model forecast

	Total accumulated precipitation (mm w.e.)			
Type	2015–2016 12 December 31 January	2016–2017 1 November 31 January	2017–2018 1 November 31 January	2018–2019 1 November 31 January
MRR-LPM_{OASI}	42 (58–25)	85 (109–62)	44 (57–31)	50 (68–33)
MRR-LPM_{OASI} (1min data)	\	\	43 (56–30)	50 (68–33)
MRR-TRwS	\	\	\	44 (59–28)
Souverijns (2017)	114 (221–51)	240 (446–109)	116 (189–46)	137 (249–61)
Grazioli (2017a)	38 (45–35)	59 (73–47)	23 (36–16)	34 (45–27)
ERA Interim	76 (101–51)	78 (101–54)	77 (104–50)	81 (109–52)
ERA5	81 (95–62)	106 (121–90)	71 (85–57)	106 (128–83)
Operational	86 (105–66)	105(128–82)	80 (99–62)	87 (111–63)
AMPS	53 (57–49)	54 (57–50)	40 (44–37)	42 (45–38)

Values inside the brackets represent the variability range of the data (as described in the text).

Sensitivity of regression procedure to the wind speed threshold within the selection of Ze^m and SF^m_{RATE} ensemble (see Section 3.1) has also been tested. Increase in threshold value to 9, 11, 15 and 20 m s^{-1} causes a small decrease only in the A parameter (−3, −7, −12 and −17%, respectively), with no variation in the B parameter and only a small increase of cumulative SF from +2 to +9%, respectively (not shown). Indeed, no variation in regression result is apparent using aspect ratio values of 0.4 and 0.8 (see Section 3.1).

Figure 5 also reports accumulated precipitation measured by the TRwS snow gauge over the period of co-located

https://doi.org/10.1017/jog.2020.70 Published online by Cambridge University Press

Table 3. Comparison between observations and ECMWF Operational (OP), ERA5 and ERA Interim (ERAin) and AMPS forecast products on a daily basis and for different time periods and MRR snowfall event quantity

		Total			Statistics				Contingency table			
		N	*O* mm w.e.	*M* mm w.e.	DIFF (%)	MBE mm w.e.	MAE mm w.e.	RMSE mm w.e.	Yes/Yes (%)	Yes/No (%)	No/Yes (%)	No/No (%)
MRR-TRwS	2018–2019	63	30	48	37	−0.29	0.36	1.03	42.9	1.6	0.0	55.6
MRR-TRwS	2018–2019	57	23	32	15	−0.15	0.22	0.57	43.9	1.8	0.0	54.4
OP-MRR	2015–2019	328	221	359	79	0.42	0.65	1.69	39.63	0.3	28.9	31.1
ERA5-MRR				364	82	0.43	0.64	1.68	43.96	0.3	29.5	29.6
ERAin-MRR				312	62	0.27	0.66	1.84	39.9	0.0	43.9	16.2
AMPS-MRR				189	69	−0.09	0.51	1.59	39.3	0.6	33.8	26.2

Columns represents: number of days considered (*N*); cumulative SF observed by MRR (*O*, mm w.e.); cumulative TP forecasted by model (*M*, mm w.e.); differences between MRR and models (DIFF, %); Mean Bias Error between MRR and models (MBE, mm w.e.); Mean Absolute Error between MRR and models (MAE, mm w.e.); Root Mean Square Error between MRR and models (RMSE, mm w.e.). Last four columns show the contingency table between observations and model outputs. In the first two rows, MRR is considered model (*M*) and TRwS snow gauge the Observation (*O*). The second row considers the same period of the first one but with the 3–5 December 2018 event disregarded.

measurements (1 December 2018–30 January 2019) with MRR. Raw TRwS precipitation data show a total accumulation of 93 mm w.e. Correction for false SF events, essentially connected to wind effects during non-*snowy* periods, erases ∼67% of the total, with a final cumulative value of 31 mm w.e. Regardless of the absolute value, there is a general agreement between the TRwS and MRR measurements: the contingency tables on both hourly (not shown) and daily bases (Table 3) highlight that more than 95% of the time the MRR records are in accordance with the TRwS.

4.3 Precipitation quantities at MZS from reanalysis product and model forecasts

Figure 5 shows the ECMWF (ERAin, ERA5 and OP) and AMPS accumulated TP time series. Comparison between values of estimated SF_{MRR} and the ECMWF TP shows large overestimation in accumulated quantities, +52, +72 and +71% (ERAin, ERA5 and OP, respectively) over the four campaigns. The OP forecasts highlight the larger overestimations in all campaigns (+93, +25, +61 and +74% for 2015–16, 2016–17, 2017–18 and 2018–19, respectively – Table 2) followed by ERA5 (+92, +25, +61 and +112%) and ERAin (+81, −9, +75 and +62%). Only for the 2016–2017, the ECMWF products more closely resemble the SF accumulated values computed from MRR measurements but, as mentioned above, the observed differences are principally due to the aforementioned huge event in January 2017, not well represented in the analysis. On the other hand, the AMPS accumulated TP shows a restrained underestimation of ∼−8% averaged over the four campaigns (+26, −47, −10 and −16% for 2015–16, 2016–17, 2017–18 and 2018–19 – Table 2) with respect to the MRR. During the YOPP intensive observation period in 2018–2019, the radiosounding launches, assimilated to produce analysis and reanalysis, were enhanced (from two to three launches per day at synoptical hours 00.00, 06.00 and 12.00 UTC). However, it does not seem that a clear improvement in SF quantity forecast was achieved. Indeed, the mean biases compared to the MRR are +0.4, +0.6, +0.3 and −0.09 mm w.e. for ERAin, ERA5, OP and AMPS, respectively, in line with the other three periods under examination.

A large spatial variability in TP values is also apparent in all ECMWF products when considering the four nearest grid points around MZS. This causes a large std dev. in the TP average over the four grid points enclosing the site, up to 20% on average using OP and ERA5 (17 and 23%, respectively) and 33% with ERAin, mostly due to the better horizontal resolution (see Section 5.4) of the former (0.125° × 0.125° and 0.25° × 0.25°, respectively) compared to the latter (0.75° × 0.75°). For the same reason, the AMPS dataset, based on a finest horizontal grid resolution (1 × 1 km), highlights a very small std dev. (8%) between the four points enclosing MZS.

Some discrepancy between products is also apparent when accumulated TP were evaluated over similar spatial surfaces. Products with the finest resolution show, on average, more precipitation. AMPS, OP and to a lesser extent ERA5 highlight +30, +20 and +3%, respectively, more than ERAin when their TP fields were averaged over the ERAin coarser mesh grid closer to MZS (Fig. 1). This surplus is particularly visible during seasons with high cumulative precipitation (2015–16 and 2017–18), whereas during the other studied seasons, differences are highly reduced (not shown).

On a daily basis, ERA5 and OP are more able than AMPS and ERAin to correctly reproduce the general timing of a precipitation event. Contingency table (Table 3) highlights that ERA5 and OP are ∼70% of the time in accordance with observations whereas AMPS and ERAin show less agreement (65 and 55%, respectively). However, all the considered reanalysis and model forecasts overestimate precipitation event numbers. On average, for ∼50% of the period under consideration an event is forecast, whereas the MRR observes SF only for 8% of the time. Similar behaviors appear at various time scales (hourly for ERA5 and OP and 3-hourly for ERAin, not shown), whereas no hourly statistics were computed for AMPS because only daily forecasts are available. During the 2015–2016 campaign, all models show the largest differences compared to observations, even though this campaign is characterized by a lower SF data availability (not shown).

4.4 Air masses: main path during SF events

Figure 6 shows areas preferentially overflown by air mass 1 d back-trajectories (TJ), ending hourly at 3000 m above MZS during the four campaigns. The choice is related to the MRR reflectivity profiles highlighting increases above sensitivity threshold due to particles falling at that altitude more than 30% of the time (Fig. 3a).

Color shading shows that most of TJs lie in the region between the Drygalski Ice Tongue and Mount Melbourne extending easterly over the Ross Sea, far southerly toward the Ross Ice Shelf and westerly along the plateau escarpment. The latter represents the main route of air masses that reach the site. In Figure 6, the results of the cluster analysis, applied only to ∼1300 TJs relative to SF events estimated by models, are also shown with five main paths (CL1–CL5) in evidence. CL1 represents 9% of the total TJ selected, coming from the Sea area facing MZS but intruding

https://doi.org/10.1017/jog.2020.70 Published online by Cambridge University Press

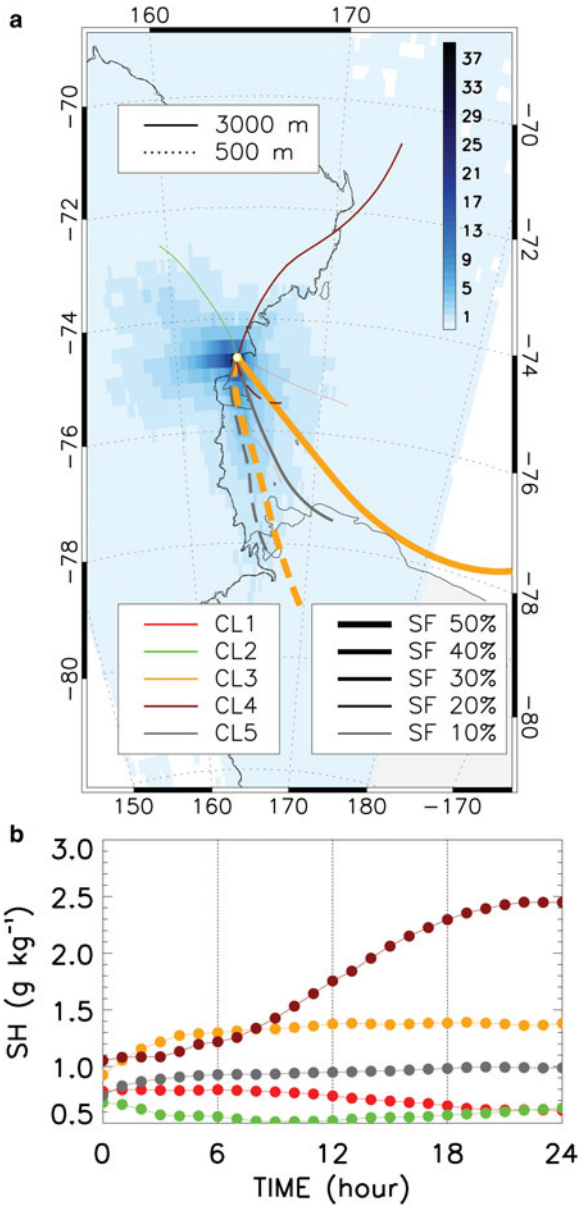

Fig. 6. The main pattern of 1 d back-trajectories ending at 3000 m over Mario Zucchelli Station. (a) The number of back-trajectories transited over each lon-lat box of 0.5° × 0.25°, during the whole period (computed hourly from 6 November to 31 January, during 2015–16, 2016–17, 2017–18 and 2018–19 summer campaigns) is reported in a blue color scale. The map is expressed in percent with respect to the number of total back-trajectories considered. Overlying, the mean trajectories, representative of each cluster obtained in the analysis, are reported in different colors. Cluster analysis is applied only to trajectories at 3000 m (solid lines) and 500 m (dashed lines) associated with snowfall events at the site (SF>0). The width of the trajectories line represents the percentage of the snowfall related to each cluster. (b) The mean specific humidity (g kg^{-1}) along the trajectory is reported, for each cluster.

over the continent more northerly or southerly from the site and reaching it from the plateau, following the Priestley and Reeves glaciers. CL2 encloses TJs (11% of the total), associated with very small SF, that lies over the continent and reaches the site toward the plateau escarpment. CL3 depicts all TJs (31% of the total) that directly arrive at the site, from the eastern part of the Ross Ice Shelf or from the southern Ross Sea, at the edge of the Ross Ice Shelf. CL4 highlights TJs coming from Indian/Pacific Oceans that intrude over Northern Victoria Land and reach the site from the plateau (11% of the total). Finally, CL5 represents the TJs, which mostly follow the Transantarctic Mountains and are channeled just south of the Drygalski Ice Tongue and Inexpressible Island, reaching MZS from the east (38% of the total). The same cluster classification implemented for TJs at 3000 m, but applied to the TJs ending at a lower altitude (1000, 1500 and 2000 m) above MZS (not shown), reveal that TJs are comprised at a higher latitude and generally come from Ross Sea/Ice Shelf to the detriment of those coming from the Southern Ocean. Finally, TJs ending at 500 m above the site show that all of the TJs fly from the south toward MZS, following the coastal line.

5. Discussion

5.1 SF comparison with snow gauge and other Ze–SF relationships

Using a Ze–SF$_{RATE}$ relationship that is not optimized for the site can cause large biases in cumulative SF$_{MRR}$. Precipitation amounts calculated by means of applying the two most recent relationships described in Souverijns and others (2017) and Grazioli and others (2017a) for PE and DDU sites, respectively, highlight large biases with respect to SF$_{MRR}$. More than triple the accumulation has been obtained by applying averaged values of the *A* and *B* parameters reported in Souverijns and others (2017) to 1 min Z_{MRR} data. However, the large variability in parameters claimed by those authors profoundly affects the results. In particular, less pronounced differences (∼+25%, not shown) are obtained using, as pre-factor *A*, the upper bound proposed by the authors, according to the fact that the coastal site conditions, associated with larger particles, are better reproduced by using a larger *A* parameter. Conversely, when SF$_{MRR}$ are calculated from 1 h Z_{MRR} data as in Grazioli and others (2017a) for DDU, differences are less pronounced compared to the one based on Souverijns and others (2017), even if an underestimation is still persistent for all the selected campaigns (∼−30%). This is partly due to the more similar precipitation conditions for two coastal sites (MZS and DDU) compared to a site such as PE located at the edge of the plateau escarpment, 150 km away from the coast.

At the end of the collocated measurement period (1 December 2018–1 February 2019), the total accumulated values of SF$_{MRR}$ are too high compared to a value for TRwS that is corrected only for false positive (∼49 and ∼31 mm w.e., respectively) with ∼+37% in favor of SF$_{MRR}$ cumulus (Table 3), even taking into account the error associated with the calculation of SF$_{MRR}$. On a daily basis, the Mean Bias Error (MBE), the Mean Absolute Error (MAE) and the Root Mean Square Error (RMSE) are −0.29, 0.36 and 1.03 mm w.e., respectively, between SF$_{MRR}$ and TRwS data. Indeed, almost half of the observed differences are connected to the SF event that occurred 3–5 December 2018 when TRwS caught only part of the event (due to high wind speed, > 15 m s^{-1}). If this event is disregarded in making the analysis, the accumulated values decrease to 32 and 24 mm w.e., respectively, with the mean difference decreased to 25%, as MBE, MAE and RMSE statistics on a daily basis. Measurements made by weighing pluviometer can be used to validate the Ze–SF$_{RATE}$ relationship calculated from LPM$_{OASI}$ disdrometer data. For the season 2018–2019, the Ze–SF$_{RATE}$ relationship can be evaluated using directly the 5 min average Z_{MRR} and TRwS SF data (Fig. 4), as in Grazioli and others (2017a). The obtained value of the *B* parameter is comparable with the one calculated with the regression procedure based on LPM$_{OASI}$ data, whereas the *A* parameter highlights some small discrepancies inside the evaluated parameter errors (Table 1). Indeed, the cumulative SF$_{MRR}$ calculated for the 2018–2019 campaign using the Ze–SF$_{RATE}$ relationship based on TRwS data (44 mm w.e.) highlights lower value (−12%, Table 2) with respect to the one calculated with the relationship based on disdrometer data.

If the correction for snow catch biases as functions of wind speed and temperature (Kochendorfer and others, 2017) is

https://doi.org/10.1017/jog.2020.70 Published online by Cambridge University Press

applied to TRwS data, difference changes sign in favor of TRwS (+3 mm w.e.) over the whole period of collocated measurements and it is even increased to +5.3 mm w.e. if the 3–5 December 2018 event is disregarded. With such changes, the recalculation of Ze–SF_{RATE} relationship using TRwS data and MRR brings a more accentuated discrepancy with the one calculated with disdrometer data. A decrease of −23 and −5% in *A* and *B*, respectively, is highlighted; but the cumulative SF at the end of the season (63 mm w.e.) shows a restrained difference of +26% with respect to SF_{MRR}, still within considered relationships errors. However, care should be taken in considering this correction because multi-site transfer function development is at an early stage of development, based only on few data obtained at few sites where validated precipitation references are available (Kochendorfer and others, 2017); further, it is still not possible to take into account all the specific site climate characteristics where the relation is applied, not to mention instrumental issues.

5.2 Synoptic moisture transport during precipitation events

Precipitation events occurring in the area of TNB are mainly driven by southward warm-air advection provided by the synoptic low-pressure centers that travel over the Ross Sea/Ross Ice Shelf and mesocyclones generally forming at the edge of the Ross Ice Shelf and moving northward or facing TNB, thanks to local interaction between the cold katabatic flow and the warmer synoptic environments over the Ross Sea (Carrasco and others, 2003; Sinclair and others, 2010). Air mass TJs for the considered precipitation events arriving at 3000 m above MZS confirm the importance of cluster CL3 which comprises more than 50% of the TP. The associated TJs come from the western Ross Sea, and they bring air of higher absolute humidity (Fig. 6b) and flow at lower altitude over the ice-free sea water for most of their path. Moreover, they undergo the most evident orographically induced updraft during the final hours of transport and consequently bring more precipitation to the site than other CLs with respect to CL1, CL2 and CL5 (not shown). Similar characteristics of thermodynamics and altitude are apparent in CL4 related to TJs lower latitude provenance but the small numbers of TJs in the cluster (11% of the total) and the few related SF (14%) probably indicate that the cluster has less importance for the site. The Ross Sea represents an important moisture source for all of Victoria Land, especially during the summer period. On the other hand, during winter months mesocyclones moving around Victoria Land show a not well-defined cloud signature connected to a lack of moisture due to the Ross Ice Shelf and the presence of sea ice inhibiting cloud formation (Carrasco and others, 2003). McCarthy Ridge is a drilling site between the Eisenhower Range and the Nansen Ice Sheet, 40 km from MZS (Fig. 1). The annual average accumulation at the site is 260 kg m^{-2} a^{-1} with a variability of 130–426 kg m^{-2} a^{-1}. Seasonal trends of isotopes and chemical species at the site confirm the contribution of summer precipitation to SMB of the area (Stenni and others, 2000). Scarchilli and others (2011) showed that Victoria Land coastal received SF atypically with respect to other Antarctica areas in terms of pathway (eastern instead of western), seasonality (summer instead of winter) and velocity (old air age). Their analysis highlighted that the Ross Sea is the provenance area of most of the air mass back-trajectories related to SF during late fall and summer at Taylor and Talos Dome drilling sites; Taylor Dome being located close to the edge of the Ross Ice Shelf and Talos Dome on the plateau in Northern Victoria Land (Fig. 1). For the same sites, Mezgec and others (2017) highlighted the importance of latent-heat polynyas in loadings of air masses through their path over the Ross Sea toward the site. Indeed, during middle December through the end of January, the Ross Sea is free of sea ice in most areas, whereas during the early summer period (October–November) there are polynyas in Ross Sea and TNB, and therefore extensive ice-free areas in those places. Moreover, Sinclair and others (2013) demonstrated that large summer SF events at Whitehall Glacier in the western Ross Sea are associated with cyclonic flow around the margin of the Ross Sea and suggest that air mass intrusions from West Antarctica may affect stable isotope ratios measured in the ice core drilled at the site.

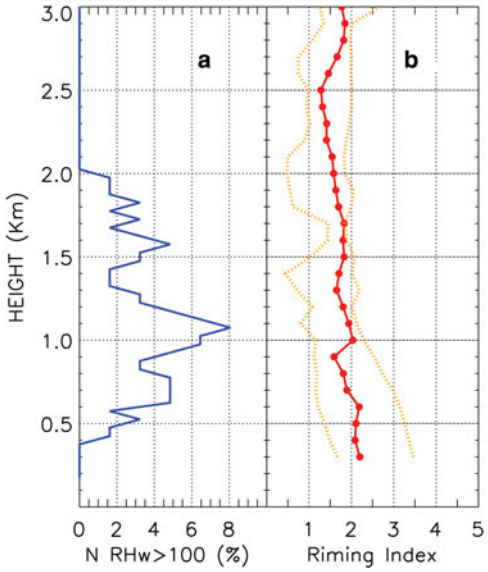

Fig. 7. (a) Number of events (%) for relative humidity with respect to water (RHw) ≥100% for each profile height levels as measured by radiosounding launched during precipitation events. (b) Median, 10 and 90 percentile values profile (red thick and orange dotted lines, respectively) of riming index calculated as Mosimann (1995) using mean fall velocity (*W*) sampled by MRR radar during the co-located radiosounding launches used in (a). Scale values on *x*-axis represent the degree of riming (1 = lightly rimed, 2 = moderately rimed, 3 = densely rimed, 4 = heavily rimed and 5 = graupel).

5.3 Interaction between precipitation and local flow

When moisture is transported to the region above the site, the thermodynamic conditions along the profile above MZS promote precipitation formed by small aggregates or single crystals. During events, profile temperature between 1 and 3 km a.s.l. ranges between −10 and −25 °C and supersaturation with respect to ice larger than 0.15 g m^{-3} occur, representing the most favorable conditions for dendrite and stellar sectored plate crystal habit growth (Bailey and Hallett, 2009). This is in good accordance with visual observation and disdrometer at the surface that report few cases of snow/ice grains but rather mostly SF with maximum median particle diameters of a few mm (Fig. 2). Moreover, a general increase of radar reflectivity between 1.5 and 2 km a.s.l. (Fig. 3b) suggests an increase in hydrometeor concentration or size, probably due to aggregation, vapor deposition or riming. No remote-sensing instrumentation at ground level was available to detect liquid phase during any of the four campaigns. However, the presence of water in liquid phase influencing the growth of particles cannot be excluded, in accordance with various authors who report the extensive presence of supercooled liquid particles over the Ross Sea area, especially during summer and autumn (Scott and Lubin, 2014; Listowski and others, 2019). At least 10% of the radiosounding launched during concomitant precipitation events show that there is a saturated layer with respect to water (RHw ≥ 100%) mostly comprised between 500 and 2000 m above the surface where temperature is always between 0 and −20 °C (Fig. 7a). Moreover, a certain degree of riming along the

https://doi.org/10.1017/jog.2020.70 Published online by Cambridge University Press

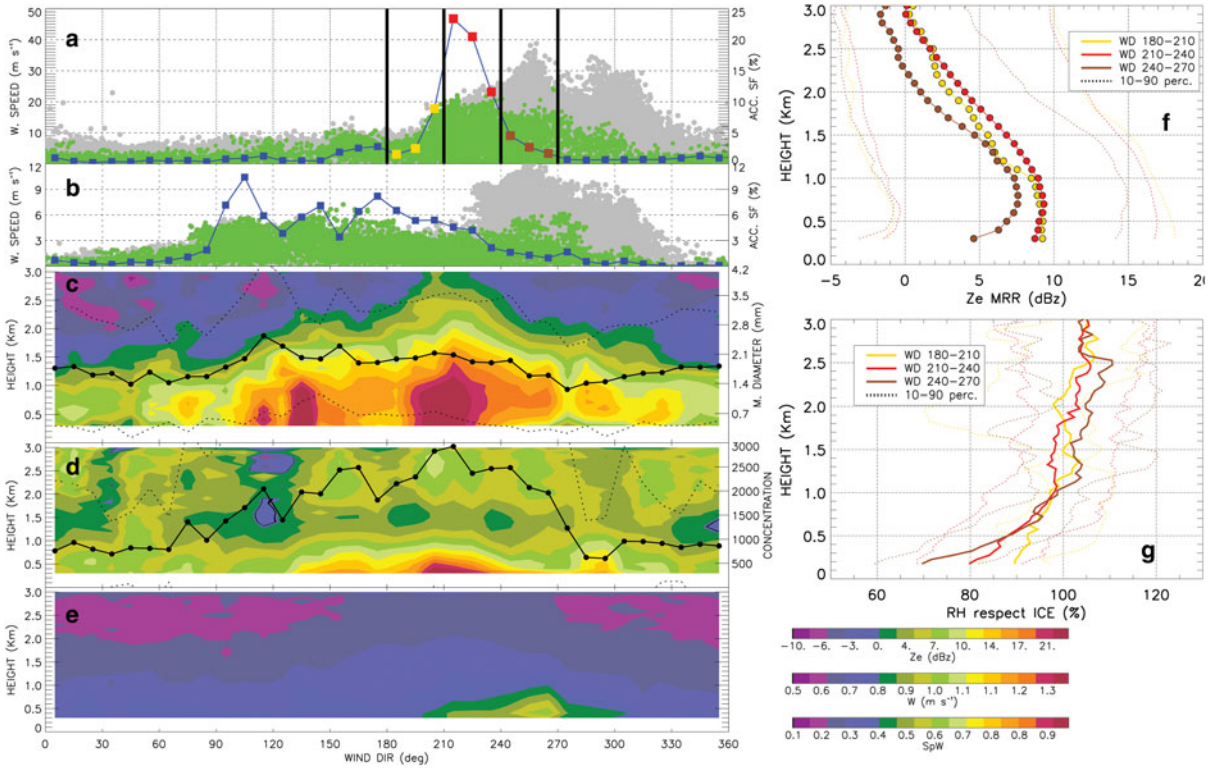

Fig. 8. SF and various MRR product profiles with respect to wind direction (WD). (a) Gray points represent all the AWS Eneide measurements of wind speed (WS, m s^{-1}) plotted with respect to WD (deg); green dots correspond to precipitation events highlighted by MRR (Z_{MRR}>−5 dB). Black line represents the quantity of precipitation calculated with relationship using MRR radar reflectivity measured at 300 m (SF_{MRR}), accumulated within each WD bin of 10° width, with respect to total accumulated SF_{MRR} (%). Dots in color refer to the corresponding values for 180°–210° (yellow), 210°–240° (red) and 240°–270° (brown) as in (f, g). (b) As in (a), but referred to the AWS Lucia. (c) Contour plot of the median profiles of radar reflectivity sampled by MRR (Ze, dBz) within each Eneide WD bin. Average median diameter (*D*0) and its std dev. for each LPM_{OASI} spectrum within each Eneide WD bin (thick and dotted line, respectively). (d) Contour plot of the mean Doppler velocity profiles sampled by MRR (W, m s^{-1}) and averaged for each Eneide WD bin. Average total number of particles and its std dev. detected by LPM_{OASI} data within each Eneide WD bin (thick and dotted line, respectively). (e) Contour plot of the mean spectral width profiles sampled by MRR (SpW) averaged within each Eneide WD bin. (f) Median profiles of radar reflectivity sampled by MRR within the Eneide WD bins (190°–210°, 210°–240° and 240°–270°) marked with yellow, red and brown as in (a). Dotted lines represent 10–90 percentiles for each median. (g) As in (f), but referred to median relative humidity with respect to ice (RHi, %) profiles from radiosounding averaged in the function of 190°–210°, 210°–240° and 240°–270° WD bins (yellow, orange and brown lines, respectively).

profiles can be inferred from a qualitative index based on the Radar W measurements (Mosimann, 1995). The method highlights a large range of conditions with a median value of ∼2 suggesting moderate riming. Also, at the 90th percentile, the index assumes the value of ∼3, implying profiles with densely rimed particles especially in the lowermost part of the radar profiles where the presence of a layer saturated with respect to water is maxima (Fig. 7b).

At the surface in summer, the area around MZS is characterized by wind, generally coming from 240° to 300° with two relative maxima at 270° and 300° (Fig. 8a) connected to the two principal katabatic drainage flows toward the sea, respectively, through the Reeves and the Priestley glaciers (Argentini and Mastrantonio, 1994; Frezzotti, 1998). During the approaches of eddies, air masses are not able to pass the Transantarctic Mountains, so a barrier wind system is established (Parish and others, 2006), with mean surface WD flowing mostly parallel to the local coastline (see clusters for TJ arriving at 500 m above the site, Fig. 6). Surface winds at MZS turn from 240°–300° to 210°–240° with more than 70% of SF_{MRR} highlighted by MRR coming from this WD range (Fig. 8a). Shifting of wind vector is generally apparent at the edge of the plateau with data registered from the AWS Lucia and showing a change of the WD from eastward to north-north/eastward, i.e. from ∼270° to 200°–100° (Fig. 8b). During precipitation, wind speed can reach up to 20 m s^{-1} at MZS and 10 m s^{-1} at Lucia, speeds that are always lower than the most intense katabatic events that occur in the area, up to 50 m s^{-1} at MZS (Fig. 8a). At the surface (up to 1 km), the barrier and the dominant downhill wind paths seem to interfere with each other. Argentini and Mastrantonio (1994) and Argentini and others (1995) highlighted that the interaction between the two flows driven by the complex orography is characteristic of the area during the summer season. Figures 8c–e show MRR variable profiles (Ze, *W* and SpW) averaged with respect to 10° bins of Eneide WD. When the effect of katabatic wind is lower, the flow generally comes between 180° and 240°.

The *W* and the Ze start to increase at a higher level with maximum values at the lowest height detectable by MRR (Figs 8c, d). This reflects the presence, on average, of larger and faster hydrometeors reaching the ground (Figs 8c, d). Similar conditions in *W* and Ze are also reported for the DDU site in some particular cases (Duràn-Alarcòn and others, 2019). On the other hand, when katabatic flow is stronger, WD comes from 210°–270°; the flow is then more turbulent (Parish and others, 1993) with an increase in the sampled spectral width and decrease in concentration (Fig. 8e). In this environment, particle sublimation increases, with a decrease in Ze and particle diameter at the lowest level (Fig. 8b). A sublimation effect is apparent in mean radiosounding profiles launched during SF events (Fig. 3b) where the RHi mean profile shows a strong decrease in the last 1000–1500 m before ground. The connection between sublimation and WD is even more evident if the RHi profiles are averaged as a function of three different surface WD bins (5, 30 and 9 profiles used for 180°–210°, 210°–240° and 240°–270° WD bins, respectively) with a sub-saturated layer enhanced in the first 1000 m above the ground for cases with WD at the surface tending toward

https://doi.org/10.1017/jog.2020.70 Published online by Cambridge University Press

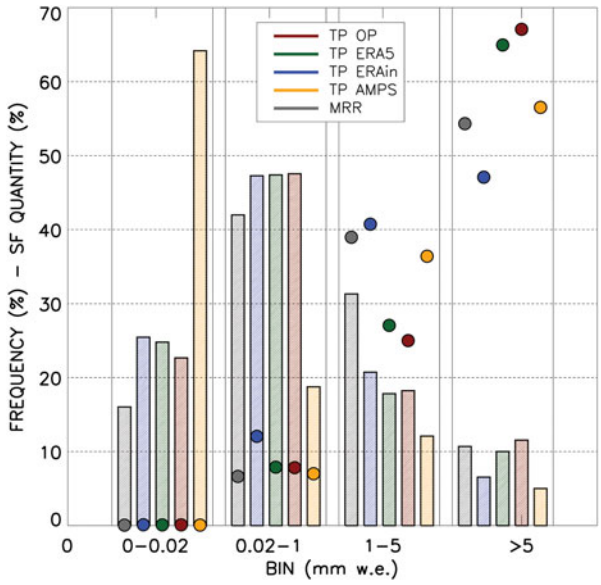

Fig. 9. Comparison between observations and models. Frequency (%, dashed bars) and quantities (%, filled points) of model total precipitation (TP) cumulated on a daily basis, grouped for events from 0 to 0.02, 0.02–1, 1–5, >5 mm w.e.; gray, red, green, blue and orange are referred to MRR, Operational (OP), ERA5, ERA Interim (ERAin) and AMPS, respectively.

270° and limited to those with WD tending toward 150° (Fig. 8g). Grazioli and others (2017b) describe the sublimation effect on falling snow particles when they precipitate within a katabatic flow at DDU. Calculated total SF profiles at MZS show similar behaviors to DDU, however influence of sublimation is lower. Mass loss can be estimated as ∼9% of the total SF precipitated during the four summers from the decrease between the maximum SF at 500 m and the reference value at 300 m above the ground. A similar result was previously reported by Souverijns and others (2018) using Ze sampled by the same MRR but for a different period and converted to SF with a different Ze–SF relationship. Our findings are also in agreement with the results of Agosta and others (2019), based on the analysis of the MAR model outputs initialized with a very high-resolution orography description (∼5 km), who proposed a light influence of sublimation over SF profiles in the TNB area. Cumulative SF profiles associated with direction bins between 180° and 240°, bringing the most part of SF amount, show that the more the wind shifts toward a southerly source direction, the less the sublimation effect is visible in the lower layers above the ground (Fig. 8g) even if a slight decrease in Ze is apparent for all WD ranges.

At higher levels above MZS, air masses from the ocean are sometimes able to move inland over the steeply sloped coastal terrain, rising altitudinally as they progress and intruding warm air masses toward the plateau. The change in air mass direction is evident in the average WD profile from radiosonde, as the air masses veer toward 180° in the first 1500 m above ground (Fig. 2b). A decrease of the MRR mean Doppler velocity profile is apparent between 1 and 2 km of altitude probably due to vertical turbulent effect generated by this vertical wind vector shift. Decrease in W is apparent in almost all of the WD spectrum but enhanced for WD coming from the sea (90°<WD<200°, Fig. 8c). When air intrusion is sufficiently strong to allow the air masses to reach the plateau, WD at AWS Lucia shows an additional variation (0–90°) with respect to the prevalent WD (100°–200°) associated to precipitation events (green dots, Fig. 8b) and the mean W profiles, as a function of the WD at Lucia, also highlight a large decrease between 1 and 1.5 km above MZS (not shown).

5.4 Performance of reanalysis and model forecast

Precipitation from reanalysis and model forecast depends only on model characteristics because the scheme is not constrained by observations. In particular, the microphysics scheme and the spatial horizontal resolution play a fundamental role in SF forecast. Surprisingly, the older reanalysis ERAin still seems to better reproduce the TP quantities at MZS than the newer reanalysis and the OP, when taking into account comparison with one point data. On a daily basis, the MBE with respect to the SF_{MRR} is lower for ERAin (0.24 mm w.e.) than the other two products (0.39 mm w.e. for ERA5 and 0.38 mm w.e. for OP), even if all the ECMWF products show the analogous frequency distribution of error magnitudes with very similar RMSE (between 1.7 and 1.9 mm w.e.). The complex orography of the TNB area is not clearly resolved by the low horizontal spatial resolution (∼80 km; Fig. 1a). Moreover, the ERAin cloud scheme is based on the 'Tiedtke' scheme (Tiedtke, 1993) with only three moisture-related prognostic variables, and, more important, on the parameterization for the precipitation phase and quantity, which are in ERAin diagnostic variables. ERAin outputs show that 10–12% of total estimated precipitation is liquid. This issue is apparent for the entire Antarctic continent but is most prominent in the coastal areas because in ERAin, when mixed precipitation occurs, the liquid fraction of precipitation is taken into account in the liquid variable (Palerme and others, 2017a). Dividing SF into various classes on a daily basis, Figure 9 highlights that ERAin and ERA5 (less for OP) both forecast too much 'extremely light' SF (<0.02 mm w.e.) with respect to the MRR. The upper limit of this bin is used, as in Turner and others (2019), as the threshold for disregarding real precipitation from spurious signals produced by the reanalysis and model forecast. ERAin forecasts 'very light' precipitation events (<1 mm w.e.) more frequently than the SF_{MRR} (+3–4%) while the number of events classified as 'light' ($1 < SF < 5$ mm w.e.) and 'heavy' (SF > 5 mm w.e.) precipitations is lower (−10 and −4%, respectively). This feature has been previously noted by Grazioli and others (2017a) for DDU and Souverijns and others (2018) for MZS, where an excessive number of low-intensity precipitation events appeared in the ERAin time series. Moreover, at DDU, the overestimation of occurrence partly compensates for the underestimation of the most intense SF events (Grazioli and others, 2017a). This is true also for MZS where, for heavier SF (>5 mm w.e.), the differences in absolute quantities are ∼−25% and partly counteract the +288 and +66% for the 'very light' and 'light' precipitation bins.

On the other hand, the OP and ERA5 have a narrower grid (∼10 and ∼31 km, respectively; Fig. 1a). Their cloud scheme is based on a more complex set of six moisture-related prognostic variables (Forbes and others, 2003; 2011) where precipitation quantities are explicitly calculated with assumptions about the particle size distribution, mass–diameter and mass–terminal velocity relationships. The improvements applied to the horizontal resolution and cloud scheme should make new product more reliable than ERAin; overall Vignon and others (2019a) showed that ERA5 better compares with radiosonde data, at MZS and other Antarctic sites, than the older reanalysis even if significant biases remain, particularly for the wind speed and relative humidity in katabatic regions. However, these changes influence the precipitation forecast in a non-straightforward way. ERA5 and OP show negligible liquid precipitation quantity in contrast with ERAin, but in accordance with the visual observations done at MZS. ERA5 and OP still overestimate the number of 'very light' SF (<1 mm w.e.). The changes introduced between ERAin and ERA5 and OP cause an increase of 3–5% in 'heavy' precipitation events and a decrease of 2–3% in 'light' precipitation events

https://doi.org/10.1017/jog.2020.70 Published online by Cambridge University Press

(SF > 5 and 1 < SF < 5 mm w.e., respectively, Fig. 9) with respect to ERAin. However, despite these modest variations, the newer versions of the IFS model tend to overestimate precipitated quantities with respect to MRR over the entire SF spectrum range. The issue is greatest for SF > 5 mm w.e. in contrast to ERAin. Indeed the 'heavy' precipitations assume a much more dominant role increasing its weight over total accumulated values from ∼45% in ERAin to more than 65% in ERA5 and OP. However, comparison with MRR only for SF > 5 mm w.e. shows that the OP and ERA5 seem to perform slightly better than ERAin with lower values of MBE and RMSE. Turner and others (2019) point out the importance of stronger precipitation events over Antarctica because they contribute greatly to the annual SF across the Antarctic continent and are the primary factors in controlling the interannual variability of accumulation. Moreover, this is particularly true in the Victoria Land area where the particular orographic conditions connect the snow accumulation to a few large SF events (Sinclair and others, 2010; Turner and others, 2019).

AMPS seems to perform better than ECMWF for predicting total accumulated precipitation (Table 3), probably because of its finer horizontal resolution. Statistics are superior in the results from AMPS, with smaller systematic bias (MBE = −0.14 mm w.e.) and fewer events with a large difference from the observations (RMSE ∼1.7 mm w.e. – Table 3). As for the new ECMWF products, the polar WRF used in AMPS runs with a microphysics scheme based on five prognostic variables (WSM, Hong and others, 2004). Vignon and others (2019b) showed that polar WRF simulations, based on different state-of-the-art microphysical schemes, for two summertime precipitation events at DDU, show large discrepancies with respect to observations. Also, for results from MZS, some differences appear compared to the observations. Looking at the frequency of SF bins (Fig. 9), it forecasts too many events in the 'extremely light' SF bin, with a value more than double that of the ECMWF and MRR and having an opposite behavior in the 'very light' and 'light' SF bins with, probably, a number of events that is too small. AMPS also underestimates the number of events relative to the MRR for SF > 5 mm w.e. even if the weight over the total SF quantity is similar to the observations. In terms of SF quantities, AMPS produce a small surplus of precipitation for bins in the ranges 0.02 < SF < 5 mm w.e., with low positive bias (MBE = 0.02 and 0.14 mm w.e.) and restrained values of RMSE and MAE with respect to ECMWF products. On the other hand, over the last bin (SF > 5 mm w.e.), a strong underestimate appears (MBE = −3.8 mm w.e.) with a decrease in forecast performance confirmed by a strong increase in MAE and RMSE compared to the ECMWF and AMPS statistics calculated for SF < 5 mm (not shown).

Understanding why models do not properly forecast SF is beyond the scope of the paper, but it is still possible to put forth a hypothesis and some general statements. AMPS forecasts SF < 5 mm w.e. better than ECMWF. Most 'very light' and 'light' SF events are connected to TJs associated with CL5 (not shown), and the air masses collected over the Ross Ice Shelf are slightly colder and drier than those flowing toward the steeply sloping coasts of Victoria Land from western Ross Sea. Along this narrow and delimited path, the orographic effect induced by the Transantarctic Mountains on moist air masses is expected to be better represented in AMPS thanks to its finer spatial grid than in the lower resolution ECMWF products. On the other hand, all the models that are considered highlight non-negligible inconsistencies in forecasting larger SF events. The issue could be due to their difficulties in properly forecasting cloud thermodynamic properties in Antarctic environments. Listowski and Lachlan-Cope (2017) and Vignon and others (2019b) pointed out the difficulties of polar WRF, when running with various parameterization schemes, to give acceptable results in Antarctic coastal areas. Also, the new ECMWF microphysical scheme still did not forecast adequately some important characteristics of clouds, especially at higher latitudes (Forbes and Ahlgrimm, 2014). Consequently, the improvement of microphysical scheme is a fundamental step in order to increase precipitation prediction capabilities of meteorological models, especially at high latitude. New measurements, able to describe processes occurring within clouds, are vital in order to better understand phenomena and to validate future parametrizations. In this contest, MZS, with the instrumentation presented in this paper, could be an important site because the lower atmosphere characteristics can be considered to be representative of the coastal area of Victoria Land and part of the Ross Ice Shelf (see Figure 11 in Vignon and others, 2019a).

6. Summary and conclusions

In the present paper, co-located measurements of a vertically pointing radar (MRR, Metek), laser disdrometer (LPM_{OASI}, Thies CLima), weighing snow gauge (TRwS, MPS System), radiosoundings and AWS, carried out at the Italian Antarctic MZS, were collected over summer months (November–December–January) during four Italian Antarctic expeditions (2015–16, 2016–17, 2017–18 and the WMO YOPP Southern Hemisphere intensive campaign 2018–19). The purpose of these measurements was to quantify the SF on the ground, to evaluate the abilities of various atmospheric reanalysis and to correctly forecast precipitation quantities, and to better describe interaction between precipitation and local flow during precipitation events. Precipitation at the MZS is evaluated using a relationship between radar reflectivity (Ze) and precipitation rate (SF_{RATE}) calculated from disdrometer data spectra at the ground and using a parametric approach, in order to minimize the differences between the reflectivity measured by radar at 300 m and that one calculated from disdrometer. The most suitable relationship obtained for the MZS site is $Ze = 54 \cdot SF_{RATE}^{1.15}$. Summer mean accumulated precipitation calculated from the radar reflectivity measurements through the Ze–SF_{RATE} relation for the four campaigns considered is 55 mm w.e., with a large variability (40–85 mm w.e.) that is due to a few huge events that occurred randomly during the period. Error in amount of precipitation, derived from the relationship, is high (up to ∼40%), but in line with the results presented in previous papers based on similar data, and mostly dependent on the variability in radar reflectivity and on the inability of the disdrometer to estimate the velocities of real particles.

For the 2018–2019 summer season, a weighing snow gauge was installed in order to explore the reliability of the radar-based SF estimation. The amounts measured and calculated agree within error. If an additional correction is applied to improve snow catch bias in the snow gauge experimental data, the differences between observed and calculated SF can be further minimized. However, it is not assured that functions developed for and applied to instrumental data for other sites with different climatic conditions would be suitable for this or other Antarctic sites.

SF at the site is related to air masses coming from the Ross Ice Shelf, flowing parallel to the Victoria Land coasts and from the western Ross Sea area, with the latter moving mostly at a lower altitude, with a higher moisture content and on average bringing more precipitation. Previous papers have demonstrated that snow particles falling within the subsaturated wind flux are affected by sublimation, with a consequent decrease of precipitation quantities in the last few hundred meters near the ground. However, joint analysis of radar products and data from AWS highlight large variability in sublimation effect as a function of WD pattern.

https://doi.org/10.1017/jog.2020.70 Published online by Cambridge University Press

At the low level, the main wind flow, coming from the plateau toward the Reeves/Priestley Glaciers, interacts with the barrier wind system, established by cyclonic eddy disturbances in the Ross Sea. Until the katabatic overwhelms the barrier winds, the wind vector at MZS assumes a direction more easterly (210°–270°), and the SF particles are sublimated in the turbulent flow. In contrast, when surface wind flow is more parallel to the coast (180°–240°), sublimation effect is less pronounced.

Comparison between SF calculated from MRR data and output from three ECMWF (operational, ERAin and ERA5 Forecast) and WRF AMPS shows that all the products are able to forecast the right timing of each SF event measured on a daily basis. None of the ECMWF products adequately reproduce the total accumulation obtained during the four campaigns: the products make large overestimations of up to 100% for an individual campaign.

Even if both Operational and ERA5 have a finer spatial resolution and a new cloud scheme with a full single-moment treatment of precipitation species, they show a large departure from total cumulated precipitation calculated with MRR data (on average ∼60% for both). On the other hand, the older ECMWF reanalysis archive (ERAin) still gives better results with lower differences. However, ERAin shows a non-negligible liquid phase component in the accumulated precipitation amount in (∼10%), which is not present in visual observations, nor present in the other products. All of the considered ECMWF products overestimate 'very light' ($0.02 < SF < 1$ mm w.e.) and 'light' precipitation ($1 < SF < 5$ mm w.e.) but for the 'heavy' events ($SF > 5$ mm w.e.), Operational and ERA5 show overestimation, with respect to MRR, where ERAin highlights underestimation. On the other hand, WRF AMPS forecasts better reproduce the total accumulated precipitation with respect to the ECMWF even if it slightly underestimates the total cumulus compared to quantities calculated with the Ze–SF_{RATE} relation. AMPS benefits from its finer grid resolution in having a good ability to forecast 'light' precipitation, although it commonly makes a slight overestimation. However, AMPS shows a less good ability to forecast intense events, which it substantially underestimates.

Precipitation is a fundamental element in the hydrological cycle of the Antarctic continent but at present quantitative measures are sparse and not representative of all conditions present on the Antarctic continent. This study is a first step to present a measurement site and a methodology for quantifying the precipitation for a rugged, jagged and windy area such as the coast of the Victoria Land. There is still much effort to be done in order to project this work in a more wider context. It will be necessary, firstly to fully understand the peculiar atmospheric characteristics during precipitative phenomena in the area; secondly to find out similarities and differences between other Antarctic regions where similar studies have already been developed. In this framework, planned future studies will be focused on the quantification of the annual precipitation (both summer and winter) with the development of a climatology of the area based on at least 5 years of data (2015–present) and on the improvement of the understanding of the real impact of precipitation on the SMB in an area strongly interested by wind-related post-deposition phenomena.

Acknowledgements. This work is carried out in the framework of the MALOX (MAss LOst in wind fluX) and the APP (Antarctic Precipitation Properties) projects funded by the Italian National Antarctic Program (PNRA). This is also a contribution to the Year of Polar Prediction (YOPP), a flagship activity of the Polar Prediction Project (PPP), initiated by the World Weather Research Programme (WWRP) of the World Meteorological Organization (WMO). We acknowledge the WMO WWRP for its role in coordinating this international research activity. Meteorological and part of precipitation data were obtained from 'Meteo-Climatological Observatory at MZS and Victoria Land' of PNRA (http://www.climantartide.it). Visual observations were obtained from the Operational Meteorology Service of ENEA UTA-LOG (Antarctic Technical Unit – Logistics Service) in the framework of PNRA (www.enea.uta.it). The ECMWF Era Interim, Era5 and Operational Forecast model data were downloaded from https://apps.ecmwf.int/mars-catalogue/. The AMPS forecast data were downloaded from https://www.earthsystemgrid.org/project/amps.html. The authors wish to thank the Antarctic Technical Unit of ENEA for the logistic support to the projects and Dr M. Maahn for the useful suggestions in setting up the Micro Rain Radar system. The authors are grateful to Todd King Hinkley for his helpful support in both the discussion and the English form, which improved the quality of the paper.

References

Adhikari L, Wang Z and Deng M (2012) Seasonal variations of Antarctic clouds observed by CloudSat and CALIPSO satellites. *Journal of Geophysical Research* **117**, D04202. doi:10.1029/2011JD016719.

Agosta C and 11 others (2019) Estimation of the Antarctic surface mass balance using the regional climate model MAR (1979–2015) and identification of dominant processes. *The Cryosphere* **13**, 281–296. doi:10.5194/tc-13-281-2019.

Argentini S, Del Buono P, Della Vedova AM and Mastrantonio G (1995) A statistical analysis of wind in Terra Nova Bay, Antarctica, for the Austral summers 1988 and 1989. *Atmospheric Research* **39**, 145–156. doi:10.1016/0169-8095(95)00009-G

Argentini S and Mastrantonio G (1994) Barrier winds recorded during two summer Antarctic campaigns and their interaction with the katabatic flows as observed by try axial Doppler sodar. *International Journal of Remote Sensing* **15**(2), 455–466. doi:10.1080/01431169408954086

Atlas D, Srivastava RC and Sekhon RS (1973) Doppler Radar characteristics of precipitation at vertical incidence. *Reviews of Geophysics and Space Physics* **11**, 1–35. doi:10.1029/RG011i001p00001

Bailey MP and Hallett J (2009) A comprehensive habit diagram for atmospheric ice crystals: confirmation from the laboratory, AIRS II, and other field studies. *Journal of the Atmospheric Sciences* **66**, 2888–2899. doi:10.1175/2009JAS2883.1

Battaglia A, Rustemeier E, Tokay A, Blahak AU and Simmer C (2010) PARSIVEL Snow observations: a critical assessment. *Journal of Atmospheric and Oceanic Technology* **27**, 333–344. doi:10.1175/2009JTECHA1332.1

Brandes EA, Ikeda K, Zhang G, Schönhuber M and Rasmussen RM (2007) A statistical and physical description of hydrometeor distributions in Colorado snowstorms using a video disdrometer. *Journal of Applied Meteorology and Climatology* **46**, 634–650. doi:10.1175/JAM2489.1

Bromwich DH, Nicolas JP and Monaghan AJ (2011) An assessment of precipitation changes over Antarctica and the Southern Ocean since 1989 in contemporary global reanalyses. *Journal of Climate* **24**, 4189–4209. doi:10.1175/2011JCLI4074.1

Bromwich DH, Otieno FO, Hines KM, Manning KW and Shilo E (2013) Comprehensive evaluation of Polar Weather Research and Forecasting Model performance in the Antarctic. *Journal of Geophysical Research: Atmospheres* **118**, 274–292. doi:10.1029/2012JD018139

Carrasco JF, Bromwich DH and Monaghan AJ (2003) Distribution and characteristics of mesocyclones in the Antarctic: Ross Sea eastward to the Weddell Sea. *Monthly Weather Review* **131**(2), 289–301. doi:10.1175/1520-0493(2003)131<0289:DACOMC>2.0.CO;2

Chen B, Wang J and Gong D (2016) Raindrop size distribution in a midlatitude continental squall line measured by Thies optical disdrometers over east China. *Journal of Applied Meteorology And Climatology* **55**, 621–634. doi:10.1175/JAMC-D-15-0127.1

Dee DP and 34 others (2011) The ERA-Interim reanalysis: configuration and performance of the data assimilation system. *Quarterly Journal of the Royal Meteorological Society* **137**, 553–597. doi:10.1002/qj.828

Draine BT and Flatau PJ (1994) Discrete-dipole approximation for scattering calculations. *Journal of the Optical Society of America A: Optics and Image Science* **11**(4), 1491–1499. doi:10.1364/JOSAA.11.001491

Durán-Alarcón C and 7 others (2019) The vertical structure of precipitation at two stations in East Antarctica derived from micro rain radars. *The Cryosphere* **13**, 247–264. doi:10.5194/tc-13-247-2019

Fabry F (2015) *Radar Meteorology: Principles and Practice*. Cambridge: Cambridge University Press. doi:10.1017/CBO9781107707405

Favier V and 5 others (2017) Antarctica-regional climate and surface mass budget. *Current Climate Change Reports* **3**, 303–315. doi:10.1007/s40641-017-0072-z

Fontaine E and 7 others (2014) Constraining mass–diameter relations from hydrometeor images and cloud radar reflectivity in tropical continental and oceanic convective anvils. *Atmospheric Chemistry and Physics* **14**, 11367–11392. doi:10.5194/acp-14-11367-2014

Forbes RM and Ahlgrimm M (2014) On the representation of high-latitude boundary layer mixed-phase cloud in the ECMWF global model. *Monthly Weather Review* **142**, 3425–3445. doi:10.1175/MWR-D-13-00325.1

Forbes RM and Clark PA (2003) Sensitivity of extra-tropical cyclone mesoscale structure to the parametrization of ice microphysical processes. *Quarterly Journal of the Royal Meteorological Society* **129**, 1123–1148. doi:10.1256/qj.01.171

Forbes RM, Tompkins AM and Untch A (2011) A new prognostic bulk-microphysics scheme for the IFS. *ECMWF Technical Memo* **649**, 1–28. doi: 10.21957/bf6vjvxk.

Frasson RPM, da Cunha LK and Krajewski WF (2011) Assessment of the Thies optical disdrometer performance. *Atmospheric Research* **101**, 237–255. doi:10.1016/j.atmosres.2011.02.014

Frezzotti M (1998) Surface wind field of Victoria Land (Antarctica) from surveys of Aeolian morphologic features. *Terra Antarctica Report* **1**, 43–45.

Frezzotti M, Scarchilli C, Becagli S, Proposito M and Urbini S (2013) A synthesis of the Antarctic surface mass balance during the last 800 yr. *The Cryosphere* **7**, 303–319. doi:10.5194/tc-7-303-2013

Frezzotti M, Urbini S, Proposito M, Scarchilli C and Gandolfi S (2007) Spatial and temporal variability of surface mass balance near Talos Dome, East Antarctica. *Journal of Geophysical Research* **112**, F02032. doi:10.1029/2006JF000638

Friedrich K, Higgins S, Masters FJ and Lopez CR (2013) Articulating and stationary PARSIVEL disdrometer measurements in conditions with strong winds and heavy rainfall. *Journal of Atmospheric and Oceanic Technology* **30**, 2063–2080. doi:10.1175/JTECH-D-12-00254.1

Gorodetskaya IV and 9 others (2015) Cloud and precipitation properties from ground-based remote sensing instruments in East Antarctica. *The Cryosphere* **9**, 285–304. doi:10.5194/tcd-8-4195-2014

Grazioli J and 6 others (2017a) Measurements of precipitation in Dumont d'Urville, Adélie Land, East Antarctica. *The Cryosphere* **11**, 1797–1811. doi:10.5194/tc-11-1797-2017

Grazioli, J and 6 others (2017b) Katabatic winds diminish precipitation contribution to the Antarctic ice mass balance. *Proceedings of the National Academy of Sciences USA* **114**, 1858–10863. doi:10.1073/pnas.1707633114

Grigioni P and 9 others (2016) La Rete Di Stazioni Meteorologiche dell'Osservatorio Meteo-climatologico In Antartide, RT/2016/35/Enea.

Hersbach H and Dee D (2016) ERA5 Reanalysis is in production. *ECMWF Newsletter* **147**, 7.

Hogan RJ, Honeyager R, Tyynelä J and Kneifel SS (2017) Calculating the millimetre-wave scattering phase function of snowflakes using the self-similar Rayleigh-Gans approximation. *Quarterly Journal of the Royal Meteorological Society* **143**, 834–844. doi:10.1002/qj.2968

Hogan RJ and Westbrook CD (2014) Equation for the microwave backscatter cross section of aggregate snowflakes using the self-similar Rayleigh-Gans approximation. *Journal of the Atmospheric Sciences* **71**, 3292–3301. doi:10.1175/JAS-D-13-0347.1

Hong S, Dudhia J and Chen S (2004) A revised approach to ice microphysical processes for the bulk parameterization of clouds and precipitation. *Monthly Weather Reviews* **132**, 103–120. doi:10.1175/1520-0493(2004)132<0103:ARATIM>2.0.CO;2

Huang GJ, Bringi VN, Cifelli R, Hudak D and Petersen WA (2010) A methodology to derive radar reflectivity-liquid equivalent snow rate relations using C-band radar and a 2D video disdrometer. *Journal of Atmospheric and Oceanic Technology* **27**, 637–651. doi:10.1175/2009JTECHA1284.1

IPCC, 2013: Climate Change (2013) *The Physical Science Basis. Contribution of Working Group I to the Fifth Assessment Report of the Intergovernmental Panel on Climate Change*. Cambridge University Press, Cambridge doi:10.1017/CBO9781107415324

Kochendorfer J and 11 others (2017) The quantification and correction of wind-induced precipitation measurement errors. *Hydrology and Earth System Sciences* **21**, 1973–1989. doi:10.5194/hess-21-1973-2017

Konishi H, Muramoto K, Shiina T, Endoh T and Kitano K (1992) Z-R relation for graupels and aggregates observed at Syowa station, Antarctica. National Institute of Polar Research. *Proceedings of the NIPR Symposium on Polar Meteorology and Glaciology* **5**, 97–103.

Lemonnier F and 11 others (2019) Evaluation of CloudSat snowfall rate profiles by a comparison with in situ micro-rain radar observations in East Antarctica. *The Cryosphere* **13**, 943–954. doi:10.5194/tc-13-943-2019

Lenaerts JTM, Fyke J and Medley B (2018) The signature of ozone depletion in recent Antarctic precipitation change: a study with the Community Earth System Model. *Geophysical Research Letters* **45**, 12,931–12,939. doi:10.1029/2018GL078608

Lenaerts JTM, Vizcaino M, Fyke J, Van Kampenhout L and Van den Broeke MR (2016) Present-day and future Antarctic ice sheet climate and surface mass balance in the Community Earth System Model. *Climate Dynamics* **47**, 1367–1381. doi:10.1007/s00382-015-2907-4

Li L and Pomeroy JW (1997) Estimates of threshold wind speeds for snow transport using meteorological data. *Journal of Applied Meteorology* **36**, 205–213. doi:10.1175/1520-0450(1997)036<0205:EOTWSF>2.0.CO;2

Listowski C, Delanoë J, Kirchgaessner A, Lachlan-Cope T and King J (2019) Antarctic clouds, supercooled liquid water and mixed phase, investigated with DARDAR: geographical and seasonal variations. *Atmospheric Chemistry and Physics* **19**, 6771–6808. doi:10.5194/acp-19-6771-2019

Listowski C and Lachlan-Cope T (2017) The microphysics of clouds over the Antarctic Peninsula – Part 2: modelling aspects within Polar WRF. *Atmospheric Chemistry and Physics* **17**, 10195–10221. doi: 10.5194/acp-17-10195-2017.

Locatelli JD and Hobbs PV (1974) Fall speeds and masses of solid precipitation particles. *Journal of Geophysical Research* **79**(15), 2185–2197. doi:10.1029/JC079i015p02185

Maahn M and 7 others (2014) How does the spaceborne radar blind zone affect derived surface snowfall statistics in polar regions? *Journal of Geophysical Research. Atmospheres: JGR* **119**, 13604–13620. doi:10.1002/2014JD022079

Maahn M and Kollias P (2012) Improved micro rain radar snow measurements using Doppler spectra post-processing. *Atmospheric Measurement Technology* **5**, 2661–2673. doi:10.5194/amt-5-2661-2012

Markwardt CB (2009) Non-linear least squares fitting in IDL with MPFIT. In Bohlender D, Durand D and Dowler P*ASP Conf. Ser., Proceedings of the conference Astronomical Data Analysis Software and Systems (ADASS) XVIII*, 2–5 November 2008, Québec City, Canada, Vol. 411. San Francisco: Astronomical Society of the Pacific, p. 251.

Matrosov SY (2007) Modeling backscatter properties of snowfall at millimeter wavelengths. *Journal of Atmospheric Science* **64**, 1727–1736. doi:10.1175/JAS3904.1

Medley B and Thomas ER (2019) Increased snowfall over the Antarctic Ice Sheet mitigated twentieth-century sea-level rise. *Nature Climate Change* **9**, 34–39. doi:10.1038/s41558-018-0356-x

Mezgec K and 14 others (2017) Holocene sea ice variability driven by wind and polynya efficiency in the Ross Sea. *Nature Communications* **8**, 1334 doi:10.1038/s41467-017-01455-x

Milani L and 8 others (2018) Cloudsat snowfall estimates over Antarctica and the Southern Ocean: an assessment of independent retrieval methodologies and multi-year snowfall analysis. *Atmospheric Research* **213**, 121–135. doi:10.1016/j.atmosres.2018.05.015

Mishchenko MI, Travis LD and Mackowski DW (1996) T-matrix computations of light scattering by nonspherical particles: a review. *Journal of Quantitative Spectroscopy & Radiative Transfer* **55**, 535–575. doi:10.1016/0022-4073(96)00002-7

Molthan AL, Colle BA, Yuter SE and Stark D (2016) Comparisons of modeled and observed reflectivities and fall speeds for snowfall of varied riming degrees during winter storms on long island, New York. *Monthly Weather Reviews* **144**, 4327–4347. doi:10.1175/MWR-D-15-0397.1

Monaghan AJ and 15 others (2006) Insignificant change in Antarctic snowfall since the International Geophysical Year. *Science (New York, N.Y.)* **313**, 827–831. doi:10.1126/science.1128243

Mosimann L (1995) An improved method for determining the degree of snow crystal riming by vertical Doppler radar. *Atmospheric Research* **37**, 305–323. doi:10.1016/0169-8095(94)00050-N

Newman AJ, Kucera PA and Bliven LF (2009) Presenting the snowflake video imager (SVI). *Journal of Atmospheric and Oceanic Technology* **26**, 167–179. doi:10.1175/2008JTECHA1148.1

Palerme C and 5 others (2014) How much snow falls on the Antarctic ice sheet? *The Cryosphere* **8**, 1577–1587. doi:10.5194/tc-8-1577-2014

https://doi.org/10.1017/jog.2020.70 Published online by Cambridge University Press

Palerme C and 5 others (2017a) Evaluation of Antarctic snowfall in global meteorological reanalyses. *Atmospheric Research* **190**, 104–112. doi:10.1016/j.atmosres.2017.02.015

Palerme C and 5 others (2017) Evaluation of current and projected Antarctic precipitation in CMIP5 models. *Climate Dynamics* **48**(1), 225–239. doi:10.1007/s00382-016-3071-1

Palm SP, Kayetha V, Yang Y and Pauly R (2017) Blowing snow sublimation and transport over Antarctica from 11 years of CALIPSO observations. *The Cryosphere* **11**, 2555–2569. doi:10.5194/tc-11-2555-2017

Parish TR, Cassano JJ and Seefeldt MW (2006) Characteristics of the Ross Ice Shelf airstream as depicted in Antarctic Mesoscale Prediction System simulations. *Journal of Geophysical Research* **111**, D12109. doi:10.1029/2005JD006185

Parish TR, Pettré P and Wendler G (1993) The influence of large-scale forcing on the katabatic wind regime at Adélie Land, Antarctica. *Meteorology and Atmospheric Physics* **51**, 165–176. doi:10.1007/BF01030492

Savina M, Schäppi B, Molnar P, Burlando P and Sevruk B (2012) Comparison of a tipping-bucket and electronic weighing precipitation gauge for snowfall. *Atmospheric Research* **103**, 45–51. doi:10.1016/j.atmosres.2011.06.010

Scarchilli C and 5 others (2010) Extraordinary blowing snow transport events in East Antarctica. *Climate Dynamics* **34**, 1195–1206. doi:10.1007/s00382-009-0601-0

Scarchilli C, Frezzotti M and Ruti PM (2011) Snow precipitation at four ice core sites in East Antarctica: provenance, seasonality and blocking factors. *Climate Dynamics* **37**, 2107–2125. doi:10.1007/s00382-010-0946-4

Scott RC and Lubin D (2014) Mixed-phase cloud radiative properties over Ross Island, Antarctica: the influence of various synoptic-scale atmospheric circulation regimes. *Journal of Geophysical Research. Atmospheres* **119**, 6702–6723. doi:10.1002/2013JD021132

Sinclair KE, Bertler NAN and Trompetter WJ (2010) Synoptic controls on precipitation pathways and snow delivery to high-accumulation ice core sites in the Ross Sea region, Antarctica. *Journal of Geophysical Research* **115**, D22112 doi:10.1029/2010JD014383

Sinclair KE, Bertler NAN, Trompetter WJ and Baisden WT (2013) Seasonality of air mass pathways to coastal Antarctica: ramifications for interpreting high-resolution ice core records. *Journal of Climate* **26**, 2065–2076. doi:10.1175/JCLI-D-12-00167.1

Souverijns N and 8 others (2017) Estimating radar reflectivity – snowfall rate relationships and their uncertainties over Antarctica by combining disdrometer and radar observations. *Atmospheric Research* **196**, 211–223. doi:j.atmosres.2017.06.001

Souverijns N and 10 others (2018) Evaluation of the CloudSat surface snowfall product over Antarctica using ground-based precipitation radars. *The Cryosphere* **12**, 3775–3789. doi:10.5194/tc-12-3775-2018

Stein AF and 5 others (2015) NOAA's HYSPLIT atmospheric transport and dispersion modeling system. *Bulletin of the American Meteorological Society* **96**, 2059–2077. doi:10.1175/BAMS-D-14-00110.1

Stenni B and 6 others (2000) Snow accumulation rates in northern Victoria Land, Antarctica, by firn-core analysis. *Journal of Glaciology* **46**(155), 541–552. doi:10.3189/172756500781832774

Thomas ER and 15 others (2017) Regional Antarctic snow accumulation over the past 1000 years. *Climate of the Past* **13**, 1491–1513. doi:10.5194/cp-13-1491-2017

Tiedtke M (1993) Representation of clouds in large scale models. *Monthly Weather Reviews* **117**, 1779–1800. doi:10.1175/1520-0493(1993)121<3040:ROCILS>2.0.CO;2

Turner J and 12 others (2019) The dominant role of extreme precipitation events in Antarctic snowfall variability. *Geophysical Research Letters* **46**, 3502–3511. doi:10.1029/2018GL081517

van Wessem JM and 18 others (2018) Modelling the climate and surface mass balance of polar ice sheets using RACMO2 – part 2: Antarctica (1979–2016). *The Cryosphere* **12**, 1479–1498. doi:10.5194/tc-12-1479-2018

Vignon É, Besic N, Jullien N, Gehring J and Berne A. (2019b) Microphysics of snowfall over coastal East Antarctica simulated by Polar WRF and observed by radar. *Journal of Geophysical Research* **124**, 11452–11476. doi:10.1029/2019JD031028

Vignon É, Traullé O and Berne A (2019a) On the fine vertical structure of the low troposphere over the coastal margins of East Antarctica. *Atmospheric Chemistry and Physics* **19**, 4659–4683. doi:10.5194/acp-19-4659-2019

Yuter SE, Kingsmill DE, Nance LB and Löffler-Mang M (2006) Observations of precipitation size and fall speed characteristics within coexisting rain and wet snow. *Journal of Applied Meteorology* **45**, 1450–1464. doi:10.1175/JAM2406.1

Zhang L and 7 others (2015) Intercomparison of solid precipitation derived from the weighting rain gauge and optical instruments in the Interior Qinghai-Tibetan Plateau. *Advances in Meteorology* **2015**, 936724. doi:10.1155/2015/936724

https://doi.org/10.1017/jog.2020.70 Published online by Cambridge University Press